Multi-Band Image Fusion Based on Spectral Unmixing

Qi Wei, *Member, IEEE*, José Bioucas-Dias, *Senior Member, IEEE*, Nicolas Dobigeon, *Senior Member, IEEE*, Jean-Yves Tourneret, *Senior Member, IEEE*, Marcus Chen, *Member, IEEE*, and Simon Godsill, *Member, IEEE*

***Abstract*—This paper presents a multi-band image fusion algorithm based on unsupervised spectral unmixing for combining a high-spatial low-spectral resolution image and a low-spatial high-spectral resolution image. The widely used linear observation model (with additive Gaussian noise) is combined with the linear spectral mixture model to form the likelihoods of the observations. The non-negativity and sum-to-one constraints resulting from the intrinsic physical properties of the abundances are introduced as prior information to regularize this ill-posed problem. The joint fusion and unmixing problem is then formulated as maximizing the joint posterior distribution with respect to the endmember signatures and abundance maps. This optimization problem is attacked with an alternating optimization strategy. The two resulting sub-problems are convex and are solved efficiently using the alternating direction method of multipliers. Experiments are conducted for both synthetic and semi-real data. Simulation results show that the proposed unmixing based fusion scheme improves both the abundance and endmember estimation comparing with the state-of-the-art joint fusion and unmixing algorithms.**

***Index Terms*—Multi-band image fusion, Bayesian estimation, block circulant matrix, Sylvester equation, alternating direction method of multipliers, block coordinate descent.**

I. Introduction

Fusing multiple multi-band images enables a synergetic exploitation of complementary information obtained by sensors of different spectral ranges and different spatial resolutions. In general, a multi-band image can be represented as a three-dimensional data cube indexed by three exploratory variables (x, y, λ), where x and y are the two spatial dimensions of the scene, and λ is the spectral dimension (covering a range of wavelengths). Typical examples of multi-band images include hyperspectral (HS) images [2], multi-spectral (MS) images [3], integral field spectrographs [4], magnetic resonance spectroscopy images [5]. However, multi-band images with high spectral resolution generally suffers from the limited spatial resolution of the data acquisition devices, mainly due to physical and technological reasons. These limitations make it infeasible to acquire a high spectral resolution multi-band image with a spatial resolution comparable to those of MS and panchromatic (PAN) images (which are acquired in much fewer bands) [6]. For example, HS images benefit from excellent spectroscopic properties with several hundreds or thousands of contiguous bands but are limited by their relatively low spatial resolution [7]. As a consequence, reconstructing a high-spatial and high-spectral multi-band image from multiple and complementary observed images, although challenging, is a crucial inverse problem that has been addressed in various scenarios. In particular, fusing a high-spatial low-spectral resolution image and a low-spatial high-spectral image is an archetypal instance of multi-band image reconstruction, such as pansharpening (MS+PAN) [8] or HS pansharpening (HS+PAN) [9]. The interested reader is invited to consult the references [8] and [9] for an overview of the HS pansharpening problems and corresponding fusion algorithms. Note that in this paper, we focus on image fusion at pixel-level instead of feature-level or decision-level. The estimated image, with high-spatial and high-spectral resolutions, may then be used in many applications, such as material unmixing, visualization, image interpretation and analysis, regression, classification, change detection, etc.

In general, the degradation mechanisms in HS, MS, and PAN imaging, with respect to (w.r.t.) the target high-spatial and high-spectral image can be summarized as spatial and spectral transformations. Thus, the multi-band image fusion problem can be interpreted as restoring a three dimensional data-cube from two degraded data-cubes, which is an inverse problem. As this inverse problem is generally ill-posed, introducing prior distributions (regularizers in the the regularization framework) to regularize the target image has been widely explored [10]–[12]. Regarding regularization, the usual high spectral and spatial correlations of the target images imply that they admit sparse or low rank representations, which has in fact been exploited in, for example, [10]–[18].

In [14], a *maximum a posterior* (MAP) estimator incorporating a stochastic mixing model has been designed for the fusion of HS and MS images. In [19], a non-negative sparse promoting algorithm for fusing HS and RGB images has been developed by using an alternating optimization algorithm. However, both approaches developed in [14] and [19] require a very basic assumption that a low spatial resolution pixel is obtained by averaging the high resolution pixels belonging

This work was supported by the HYPANEMA ANR Project under Grant ANR-12-BS03-003, the Portuguese Science and Technology Foundation under Project UID/EEA/50008/2013, the Thematic Trimester on Image Processing of the CIMI Labex, Toulouse, France, under Grant ANR-11-LABX-0040-CIMI within the Program ANR-11-IDEX-0002-02 and the ERA-NET MED MapInvPlnt Project no. ANR-15-NMED-0002-02. Part of this work was presented during the IEEE FUSION 2016 [1].

Qi Wei and Simon Godsill are with Department of Engineering, University of Cambridge, CB2 1PZ, Cambridge, UK (e-mail: {qi.wei, sjg}@eng.cam.ac.uk). José Bioucas-Dias is with Instituto de Telecomunicações and Instituto Superior Técnico, Universidade de Lisboa, 1049-001, Lisboa, Portugal (e-mail: bioucas@lx.it.pt). Nicolas Dobigeon and Jean-Yves Tourneret are with IRIT/INP-ENSEEIHT, University of Toulouse, 31071, Toulouse, France (e-mail: {nicolas.dobigeon, jean-yves.tourneret}@enseeiht.fr). Marcus Chen is with School of Computer Engineering, Nanyang Technological University, Singapore (e-mail: marcuschen@pmail.ntu.edu.sg).

to the same area, whose size depends the downsampling ratio. This nontrivial assumption, also referred to as pixel aggregation, implies that the fusion of two multi-band images can be divided into fusing small blocks, which greatly decreases the complexity of the overall problem. Note that this assumption has also been used in [17], [20], [21]. However, this averaging assumption can be violated easily as the area in a high resolution image corresponding to a low resolution pixel can be arbitrarily large (depending on the spatial blurring) and the downsampling ratio is generally fixed (depending on the sensor physical characteristics).

To overcome this limitation, a more general forward model, which formulates the blurring and downsampling as two separate operations, has been recently developed and widely used [9], [10], [12], [15], [22], [23]. Based on this model, a non-negative matrix factorization pansharpening of HS image has been proposed in [22]. Similar works have been developed independently in [16], [24], [25]. Later, Yokoya *et al.* have proposed to use a coupled nonnegative matrix factorization (CNMF) unmixing for the fusion of low-spatial-resolution HS and high-spatial-resolution MS data, where both HS and MS data are alternately unmixed into endmember and abundance matrices by the CNMF algorithm [15]. A similar fusion and unmixing framework was recently introduced in [26], in which the alternating NMF steps in CNMF were replaced by alternating proximal forward-backward steps. The common point of these works is to learn endmembers from the HS image and abundances from the MS image alternatively instead of using both HS and MS jointly, leading to simple update rules. More specifically, this approximation helps to circumvent the need for a deconvolution, upsampling and linear regression all embedded in the proposed joint fusion method. While that approximation simplifies the fusion process, it does not use the abundances estimated from the HS image and the endmember signatures estimated from the MS image, thus not fully exploiting the spectral and spatial information in both images. To fully exploit the spatial and spectral information contained in HS and MS data pairs, we retain the above degradation model, but propose to minimize the cost function associated with the two data terms directly instead of decoupling the HS and MS term (fusing approximately). The associated minimization problem will be solved in a solid mathematical framework using recently developed optimization tools.

More specifically, we formulate the unmixing based multi-band image fusion problem as an inverse problem in which the regularization is implicitly imposed by a low rank representation inherent to the linear spectral mixture model and by non-negativity and sum-to-one constraints resulting from the intrinsic physical properties of the abundances. In the proposed approach, the endmember signatures and abundances are jointly estimated from the observed multi-band images. Note again that the use of both data sources for estimating endmembers or abundances is the main difference from current state-of-the-art methods. The optimization w.r.t. the endmember signatures and the abundances are both constrained linear regression problems, which can be solved efficiently by the alternating direction method of multipliers (ADMM).

The remaining of this paper is organized as follows. Section II gives a short introduction of the widely used linear mixture model and forward model for multi-band images. Section III formulates the unmixing based fusion problem as an optimization problem, which is solved using the Bayesian framework by introducing the popular constraints associated with the endmembers and abundances. The proposed fast alternating optimization algorithm is presented in Section IV. Section V presents experimental results assessing the accuracy and the numerical efficiency of the proposed method. Conclusions are finally reported in Section VI.

II. Problem Statement

To better distinguish spectral and spatial properties, the pixels of the target multi-band image, which is of high-spatial and high-spectral resolution, can be rearranged to build an $m_\lambda \times n$ matrix $\mathbf{X}$, where m_λ is the number of spectral bands and $n = n_r \times n_c$ is the number of pixels in each band (n_r and n_c represent the numbers of rows and columns respectively). In other words, each column of the matrix $\mathbf{X}$ consists of a m_λ-valued pixel and each row gathers all the pixel values in a given spectral band.

A. Linear Mixture Model

This work exploits an intrinsic property of multi-band images, according to which each spectral vector of an image can be represented by a linear mixture of several spectral signatures, referred to as endmembers. Mathematically, we have

$$\mathbf{X} = \mathbf{M}\mathbf{A} \tag{1}$$

where $\mathbf{M} \in \mathbb{R}^{m_\lambda \times p}$ is the endmember matrix whose columns are spectral signatures and $\mathbf{A} \in \mathbb{R}^{p \times n}$ is the corresponding abundance matrix whose columns are abundance fractions. This linear mixture model has been widely used in HS unmixing (see [27] for a detailed review).

B. Forward Model

Based on the pixel ordering introduced at the beginning of Section II, any linear operation applied to the left (resp. right) side of $\mathbf{X}$ describes a spectral (resp. spatial) degradation action. In this work, we assume that two complementary images of high-spectral or high-spatial resolutions, respectively, are available to reconstruct the target high-spectral and high-spatial resolution target image. These images result from linear spectral and spatial degradations of the full resolution image $\mathbf{X}$, according to the popular models

$$\begin{aligned} \mathbf{Y}_{\mathrm{M}} &= \mathbf{R}\mathbf{X} + \mathbf{N}_{\mathrm{M}} \\ \mathbf{Y}_{\mathrm{H}} &= \mathbf{X}\mathbf{B}\mathbf{S} + \mathbf{N}_{\mathrm{H}} \end{aligned} \tag{2}$$

where

- $\mathbf{X} \in \mathbb{R}^{m_\lambda \times n}$ is the full resolution target image as described in Section II-A.
- $\mathbf{Y}_{\mathrm{M}} \in \mathbb{R}^{n_\lambda \times n}$ and $\mathbf{Y}_{\mathrm{H}} \in \mathbb{R}^{m_\lambda \times m}$ are the observed spectrally degraded and spatially degraded images.
- $\mathbf{R} \in \mathbb{R}^{n_\lambda \times m_\lambda}$ is the spectral response of the MS sensor, which can be *a priori* known or estimated by cross-calibration [28].

- $\mathbf{B} \in \mathbb{R}^{n\times n}$ is a cyclic convolution operator acting on the bands.
- $\mathbf{S} \in \mathbb{R}^{n\times m}$ is a d uniform downsampling operator (it has $m = n/d$ ones and zeros elsewhere), which satisfies $\mathbf{S}^T\mathbf{S} = \mathbf{I}_m$.
- $\mathbf{N}_\mathrm{M}$ and $\mathbf{N}_\mathrm{H}$ are additive terms that include both modeling errors and sensor noises.

The noise matrices are assumed to be distributed according to the following matrix normal distributions[1]

$$\begin{aligned}\mathbf{N}_\mathrm{M} &\sim \mathcal{MN}_{m_\lambda,m}(\mathbf{0}_{m_\lambda,m}, \mathbf{\Lambda}_\mathrm{M}, \mathbf{I}_m)\\ \mathbf{N}_\mathrm{H} &\sim \mathcal{MN}_{n_\lambda,n}(\mathbf{0}_{n_\lambda,n}, \mathbf{\Lambda}_\mathrm{H}, \mathbf{I}_n)\end{aligned}$$

where $\mathbf{0}_{a,b}$ is an $a \times b$ matrix of zeros and $\mathbf{I}_a$ is the $a \times a$ identity matrix. The column covariance matrices are assumed to be the identity matrix to reflect the fact that the noise is pixel-independent. The row covariance matrices $\mathbf{\Lambda}_\mathrm{M}$ and $\mathbf{\Lambda}_\mathrm{H}$ are assumed to be diagonal matrices, whose diagonal elements can vary depending on the noise powers in the different bands. More specifically, $\mathbf{\Lambda}_\mathrm{H} = \mathrm{diag}\left[s^2_{\mathrm{H},1}, \cdots, s^2_{\mathrm{H},m_\lambda}\right]$ and $\mathbf{\Lambda}_\mathrm{M} = \mathrm{diag}\left[s^2_{\mathrm{M},1}, \cdots, s^2_{\mathrm{M},n_\lambda}\right]$, where diag is an operator transforming a vector into a diagonal matrix, whose diagonal terms are the elements of this vector.

The matrix equation (2) has been widely advocated for the pansharpening and HS pansharpening problems, which consist of fusing a PAN image with an MS or an HS image [9], [29], [30]. Similarly, most of the techniques developed to fuse MS and HS images also rely on a similar linear model [11], [15], [31]–[35]. From an application point of view, this model is also important as motivated by recent national programs, e.g., the Japanese next-generation space-borne HS image suite (HISUI), which acquires and fuses the co-registered HS and MS images for the same scene under the same conditions, following this linear model [36].

C. Composite Fusion Model

Combining the linear mixture model (1) and the forward model (2) leads to

$$\begin{aligned}\mathbf{Y}_\mathrm{M} &= \mathbf{RMA} + \mathbf{N}_\mathrm{M}\\ \mathbf{Y}_\mathrm{H} &= \mathbf{MABS} + \mathbf{N}_\mathrm{H}\end{aligned} \tag{3}$$

where all matrix dimensions and their respective relations are summarized in Table I.

TABLE I: Matrix dimension summary

Notation	Definition	Relation
m	no. of pixels in each row of $\mathbf{Y}_\mathrm{H}$	$m = n/d$
n	no. of pixels in each row of $\mathbf{Y}_\mathrm{M}$	$n = m \times d$
d	decimation factor	$d = n/m$
m_λ	no. of bands in $\mathbf{Y}_\mathrm{H}$	$m_\lambda \gg n_\lambda$
n_λ	no. of bands in $\mathbf{Y}_\mathrm{M}$	$n_\lambda \ll m_\lambda$

[1]The probability density function $p(\mathbf{X}|\mathbf{M}, \mathbf{\Sigma}_r, \mathbf{\Sigma}_c)$ of a matrix normal distribution $\mathcal{MN}_{r,c}(\mathbf{M}, \mathbf{\Sigma}_r, \mathbf{\Sigma}_c)$ is defined by

$$p(\mathbf{X}|\mathbf{M}, \mathbf{\Sigma}_r, \mathbf{\Sigma}_c) = \frac{\exp\left(-\frac{1}{2}\mathrm{tr}\left[\mathbf{\Sigma}_c^{-1}(\mathbf{X}-\mathbf{M})^T\mathbf{\Sigma}_r^{-1}(\mathbf{X}-\mathbf{M})\right]\right)}{(2\pi)^{rc/2}|\mathbf{\Sigma}_c|^{r/2}|\mathbf{\Sigma}_r|^{c/2}}$$

where $\mathbf{M} \in \mathbb{R}^{r\times c}$ is the mean matrix, $\mathbf{\Sigma}_r \in \mathbb{R}^{r\times r}$ is the row covariance matrix and $\mathbf{\Sigma}_c \in \mathbb{R}^{c\times c}$ is the column covariance matrix.

Note that the matrix $\mathbf{M}$ can be selected from a known spectral library [37] or estimated *a priori* from the HS data [38]. Also, it can be estimated jointly with the abundance matrix $\mathbf{A}$ [39]–[41], which will be the case in this work.

D. Statistical Methods

To summarize, the problem of fusing and unmixing high-spectral and high-spatial resolution images can be formulated as estimating the unknown matrices $\mathbf{M}$ and $\mathbf{A}$ from (3), which can be regarded as a joint non-negative matrix factorization (NMF) problem. As is well known, the NMF problem is non-convex and has no unique solution, leading to an ill-posed problem. Thus, it is necessary to incorporate some intrinsic constraints or prior information to regularize this problem, improving the conditioning of the problem.

Various priors have been already advocated to regularize the multi-band image fusion problem, such as Gaussian priors [10], [42], sparse representations [11] or total variation (TV) priors [12]. The choice of the prior usually depends on the information resulting from previous experiments or from a subjective view of constraints affecting the unknown model parameters [43], [44]. The inference of $\mathbf{M}$ and $\mathbf{A}$ (whatever the form chosen for the prior) is a challenging task, mainly due to the large size of $\mathbf{X}$ and to the presence of the downsampling operator $\mathbf{S}$, which prevents any direct use of the Fourier transform to diagonalize the spatial degradation operator $\mathbf{BS}$. To overcome this difficulty, several computational strategies, including Markov chain Monte Carlo (MCMC) [10], block coordinate descent method (BCD) [45], and tailored variable splitting under the ADMM framework [12], have been proposed, both applied to different kinds of priors, e.g., the empirical Gaussian prior [10], [42], the sparse representation based prior [11], or the TV prior [12]. More recently, contrary to the algorithms described above, a much more efficient method, named *Robust Fast fUsion based on Sylvester Equation (R-FUSE)* has been proposed to solve explicitly an underlying Sylvester equation associated with the fusion problem derived from (3) [46]. This solution can be implemented *per se* to compute the maximum likelihood estimator in a computationally efficient manner, which has also the great advantage of being easily generalizable within a Bayesian framework when considering various priors.

In our work, we propose to form priors by exploiting the intrinsic physical properties of abundances and endmembers, which is widely used in conventional unmixing, to infer $\mathbf{A}$ and $\mathbf{M}$ from the observed data $\mathbf{Y}_\mathrm{M}$ and $\mathbf{Y}_\mathrm{H}$. More details are given in the following section.

III. Problem Formulation

Following the Bayes rule, the posterior distribution of the unknown parameters $\mathbf{M}$ and $\mathbf{A}$ can be obtained by the product of their likelihoods and prior distributions, which are detailed in what follows.

A. Likelihoods (Data Fidelity Term)

Using the statistical properties of the noise matrices $\mathbf{N}_{\mathrm{M}}$ and $\mathbf{N}_{\mathrm{H}}$, $\mathbf{Y}_{\mathrm{M}}$ and $\mathbf{Y}_{\mathrm{H}}$ have matrix Gaussian distributions, i.e.,

$$\begin{aligned} p\left(\mathbf{Y}_{\mathrm{M}}|\mathbf{M},\mathbf{A}\right) &= \mathcal{MN}_{n_\lambda,n}(\mathbf{RMA},\mathbf{\Lambda}_{\mathrm{M}},\mathbf{I}_n) \\ p\left(\mathbf{Y}_{\mathrm{H}}|\mathbf{M},\mathbf{A}\right) &= \mathcal{MN}_{m_\lambda,m}(\mathbf{MABS},\mathbf{\Lambda}_{\mathrm{H}},\mathbf{I}_m). \end{aligned} \tag{4}$$

As the collected measurements $\mathbf{Y}_{\mathrm{M}}$ and $\mathbf{Y}_{\mathrm{H}}$ have been acquired by different (possibly heterogeneous) sensors, the noise matrices $\mathbf{N}_{\mathrm{M}}$ and $\mathbf{N}_{\mathrm{H}}$ are sensor-dependent and can be generally assumed to be statistically independent. Therefore, $\mathbf{Y}_{\mathrm{M}}$ and $\mathbf{Y}_{\mathrm{H}}$ are independent conditionally upon the unobserved scene $\mathbf{X} = \mathbf{MA}$. As a consequence, the joint likelihood function of the observed data is

$$p\left(\mathbf{Y}_{\mathrm{M}},\mathbf{Y}_{\mathrm{H}}|\mathbf{M},\mathbf{A}\right) = p\left(\mathbf{Y}_{\mathrm{M}}|\mathbf{M},\mathbf{A}\right)p\left(\mathbf{Y}_{\mathrm{H}}|\mathbf{M},\mathbf{A}\right). \tag{5}$$

The negative logarithm of the likelihood is

$$\begin{aligned} &-\log p\left(\mathbf{Y}_{\mathrm{M}},\mathbf{Y}_{\mathrm{H}}|\mathbf{M},\mathbf{A}\right) \\ &= -\log p\left(\mathbf{Y}_{\mathrm{M}}|\mathbf{M},\mathbf{A}\right) - \log\, p\left(\mathbf{Y}_{\mathrm{H}}|\mathbf{M},\mathbf{A}\right) + C \\ &= \tfrac{1}{2}\left\|\mathbf{\Lambda}_{\mathrm{H}}^{-\frac{1}{2}}\left(\mathbf{Y}_{\mathrm{H}} - \mathbf{MABS}\right)\right\|_F^2 + \tfrac{1}{2}\left\|\mathbf{\Lambda}_{\mathrm{M}}^{-\frac{1}{2}}\left(\mathbf{Y}_{\mathrm{M}} - \mathbf{RMA}\right)\right\|_F^2 \\ &+C \end{aligned}$$

where $\|\mathbf{X}\|_F = \sqrt{\mathrm{trace}\left(\mathbf{X}^T\mathbf{X}\right)}$ is the Frobenius norm of $\mathbf{X}$ and C is a constant.

B. Priors (Regularization Term)

1) Abundances: As the mixing coefficient $a_{i,j}$ (the element located in the ith row and jth column of $\mathbf{A}$) represents the proportion (or probability of occurrence) of the the ith endmember in the jth measurement [27], [47], the abundance vectors satisfy the following *abundance non-negativity constraint* (ANC) and *abundance sum-to-one constraint* (ASC)

$$\boldsymbol{a}_j \geq 0 \quad \text{and} \quad \mathbf{1}_p^T\boldsymbol{a}_j = 1, \forall j \in \{1,\cdots,n\} \tag{6}$$

where $\boldsymbol{a}_j$ is the jth column of $\mathbf{A}$, $\geq$ means "element-wise greater than" and $\mathbf{1}_p^T$ is a $p\times 1$ vector with all ones. Accounting for all the image pixels, the constraints (6) can be rewritten in matrix form

$$\mathbf{A} \geq 0 \quad \text{and} \quad \mathbf{1}_p^T\mathbf{A} = \mathbf{1}_n^T. \tag{7}$$

Moreover, the ANC and ASC constraints can be converted into a uniform distribution for $\mathbf{A}$ on the feasible region $\mathcal{A}$, i.e.,

$$p(\mathbf{A}) = \begin{cases} c_{\mathbf{A}} & \text{if } \mathbf{A} \in \mathcal{A} \\ 0 & \text{elsewhere} \end{cases} \tag{8}$$

where $\mathcal{A} = \left\{\mathbf{A}|\mathbf{A} \geq 0, \mathbf{1}_p^T\mathbf{A} = \mathbf{1}_n^T\right\}$, $c_{\mathbf{A}} = 1/\mathrm{vol}(\mathcal{A})$ and $\mathrm{vol}(\mathcal{A}) = \int_{\mathbf{A}\in\mathcal{A}} d\mathbf{A}$ is the volume of the set $\mathcal{A}$.

2) Endmembers: As the endmember signatures represent the reflectances of different materials, each element of the matrix $\mathbf{M}$ should be between 0 and 1. Thus, the constraints for $\mathbf{M}$ can be written as

$$0 \leq \mathbf{M} \leq 1. \tag{9}$$

Similarly, these constraints for the matrix $\mathbf{M}$ can be converted into a uniform distribution on the feasible region $\mathcal{M}$

$$p(\mathbf{M}) = \begin{cases} c_{\mathbf{M}} & \text{if } \mathbf{M} \in \mathcal{M} \\ 0 & \text{elsewhere} \end{cases}$$

where $\mathcal{M} = \{\mathbf{M}|0 \leq \mathbf{M} \leq 1\}$ and $c_{\mathbf{M}} = 1/\mathrm{vol}(\mathcal{M})$.

C. Posteriors (Constrained Optimization)

Combining the likelihoods (5) and the priors $p\left(\mathbf{M}\right)$ and $p\left(\mathbf{A}\right)$, the Bayes theorem provides the posterior distribution of $\mathbf{M}$ and $\mathbf{A}$

$$\begin{aligned} &p\left(\mathbf{M},\mathbf{A}|\mathbf{Y}_{\mathrm{H}},\mathbf{Y}_{\mathrm{M}}\right) \\ &\propto p\left(\mathbf{Y}_{\mathrm{H}}|\mathbf{M},\mathbf{A}\right)p\left(\mathbf{Y}_{\mathrm{M}}|\mathbf{M},\mathbf{A}\right)p\left(\mathbf{M}\right)p\left(\mathbf{A}\right) \end{aligned}$$

where $\propto$ means "proportional to". Thus, the unmixing based fusion problem can be interpreted as maximizing the joint posterior distribution of $\mathbf{A}$ and $\mathbf{M}$. Moreover, by taking the negative logarithm of $p\left(\mathbf{M},\mathbf{A}|\mathbf{Y}_{\mathrm{H}},\mathbf{Y}_{\mathrm{M}}\right)$, the MAP estimator of $(\mathbf{A},\mathbf{M})$ can be obtained by solving the minimization

$$\begin{aligned} \min_{\mathbf{M},\mathbf{A}} L(\mathbf{M},\mathbf{A}) \quad \text{s.t.} \quad \mathbf{A} \geq 0 \quad \text{and} \quad \mathbf{1}_p^T\mathbf{A} = \mathbf{1}_n^T \\ 0 \leq \mathbf{M} \leq 1 \end{aligned} \tag{10}$$

where

$$\begin{aligned} L(\mathbf{M},\mathbf{A}) = &\frac{1}{2}\left\|\mathbf{\Lambda}_{\mathrm{H}}^{-\frac{1}{2}}\left(\mathbf{Y}_{\mathrm{H}} - \mathbf{MABS}\right)\right\|_F^2 \\ &+ \frac{1}{2}\left\|\mathbf{\Lambda}_{\mathrm{M}}^{-\frac{1}{2}}\left(\mathbf{Y}_{\mathrm{M}} - \mathbf{RMA}\right)\right\|_F^2. \end{aligned}$$

In this formulation, the fusion problem can be regarded as a generalized unmixing problem, which includes two data fidelity terms. Thus, both images contribute to the estimation of the endmember signatures (endmember extraction step) and the high-resolution abundance maps (inversion step). For the endmember estimation, a popular strategy is to use a subspace transformation as a preprocessing step, such as in [40], [48]. In general, the subspace transformation is learned *a priori* from the high-spectral resolution image empirically, e.g., from the HS data. This empirical subspace transformation alleviates the computational burden greatly and can be incorporated in our framework easily.

IV. Alternating Optimization Scheme

Even though problem (10) is convex w.r.t. $\mathbf{A}$ and $\mathbf{M}$ separately, it is non-convex w.r.t. these two matrices jointly and has more than one solution. We propose an optimization technique that alternates optimizations w.r.t. $\mathbf{A}$ and $\mathbf{M}$, which is also referred to as a BCD algorithm. The optimization w.r.t. $\mathbf{A}$ (resp. $\mathbf{M}$) conditional on $\mathbf{M}$ (resp. $\mathbf{A}$) can be achieved efficiently with the ADMM algorithm [49], which converges to a solution of the respective convex optimization under some mild conditions. The resulting alternating optimization algorithm, referred to as Fusion based on Unmixing for Multi-band Images (FUMI), is detailed in Algorithm 1, where $\mathrm{EEA}(\mathbf{Y}_{\mathrm{H}})$ in line 1 represents an endmember extraction algorithm to estimate endmembers from HS data. The optimization steps w.r.t. $\mathbf{A}$ and $\mathbf{M}$ are detailed below.

A. Convergence Analysis

To analyze the convergence of Algorithm 1, we recall a convergence criterion for the BCD algorithm stated in [45, p. 273].

Theorem 1 (Bertsekas, [45]; Proposition 2.7.1)**.** *Suppose that L is continuously differentiable w.r.t. $\mathbf{A}$ and $\mathbf{M}$ over the convex set $\mathcal{A}\times\mathcal{M}$. Suppose also that for each $\{\mathbf{A},\mathbf{M}\}$, $L(\mathbf{A},\mathbf{M})$*

Algorithm 1: Multi-band Image Fusion based on Spectral Unmixing (FUMI)

Input: $\mathbf{Y}_{\mathrm{M}}$, $\mathbf{Y}_{\mathrm{H}}$, $\mathbf{\Lambda}_{\mathrm{M}}$, $\mathbf{\Lambda}_{\mathrm{H}}$, $\mathbf{R}$, $\mathbf{B}$, $\mathbf{S}$

/* Initialize $\mathbf{M}$ */

$\mathbf{M}^{(0)} \leftarrow \mathrm{EEA}(\mathbf{Y}_{\mathrm{H}})$;

for $t = 1, 2, \ldots$ **to** *stopping rule* **do**

  /* Optimize w.r.t. $\mathbf{A}$ using ADMM (see Algorithm 2) */

  $\mathbf{A}^{(t)} \in \arg\min_{\mathbf{A}\in\mathcal{A}} L(\mathbf{M}^{(t-1)}, \mathbf{A})$;

  /* Optimize w.r.t. $\mathbf{M}$ using ADMM (see Algorithm 5) */

  $\mathbf{M}^{(t)} \in \arg\min_{\mathbf{M}\in\mathcal{M}} L(\mathbf{M}, \mathbf{A}^{(t)})$;

end

Set $\hat{\mathbf{A}} = \mathbf{A}^{(t)}$ and $\hat{\mathbf{M}} = \mathbf{M}^{(t)}$;

Output: $\hat{\mathbf{A}}$ and $\hat{\mathbf{M}}$

viewed as a function of $\mathbf{A}$*, attains a unique minimum* $\bar{\mathbf{A}}$*. The similar uniqueness also holds for* $\mathbf{M}$*. Let* $\left\{\mathbf{A}^{(t)}, \mathbf{M}^{(t)}\right\}$ *be the sequence generated by the BCD method as in Algorithm 1. Then, every limit point of* $\left\{\mathbf{A}^{(t)}, \mathbf{M}^{(t)}\right\}$ *is a stationary point.*

The target function defined in (10) is continuously differentiable. Note that it is not guaranteed that the minima w.r.t. $\mathbf{A}$ or $\mathbf{M}$ are unique. We may however argue that a simple modification of the objective function, consisting in adding the quadratic term $\alpha_1\|\mathbf{A}\|_F^2 + \alpha_2\|\mathbf{M}\|_F^2$, where α_1 and α_2 are very small thus obtaining a strictly convex objective function, ensures that the minima of (11) and (15) are uniquely attained and thus we may invoke the Theorem (1). In practice, even without including the quadratic terms, we have systematically observed convergence of Algorithm 1.

B. Optimization w.r.t. the Abundance Matrix $\mathbf{A}$ *(*$\mathbf{M}$ *fixed)*

The minimization of $L(\mathbf{M}, \mathbf{A})$ w.r.t. the abundance matrix $\mathbf{A}$ conditional on $\mathbf{M}$ can be formulated as

$$\min_{\mathbf{A}} \frac{1}{2}\left\|\mathbf{\Lambda}_{\mathrm{H}}^{-\frac{1}{2}}\left(\mathbf{Y}_{\mathrm{H}} - \mathbf{MABS}\right)\right\|_F^2 + \frac{1}{2}\left\|\mathbf{\Lambda}_{\mathrm{M}}^{-\frac{1}{2}}\left(\mathbf{Y}_{\mathrm{M}} - \mathbf{RMA}\right)\right\|_F^2 \quad \text{s.t.} \quad \mathbf{A} \geq 0 \quad \text{and} \quad \mathbf{1}_p^T\mathbf{A} = \mathbf{1}_n^T. \tag{11}$$

This constrained minimization problem can be solved by introducing an auxiliary variable to split the objective and the constraints, which is the spirit of the ADMM algorithm. More specifically, by introducing the splitting $\mathbf{V} = \mathbf{A}$, the optimization problem (11) w.r.t. $\mathbf{A}$ can be written as

$$\min_{\mathbf{A},\mathbf{V}} L_1(\mathbf{A}) + \iota_{\mathcal{A}}(\mathbf{V}) \text{ s.t. } \mathbf{V} = \mathbf{A}$$

where $L_1(\mathbf{A}) =$

$$\frac{1}{2}\left\|\mathbf{\Lambda}_{\mathrm{H}}^{-\frac{1}{2}}\left(\mathbf{Y}_{\mathrm{H}} - \mathbf{MABS}\right)\right\|_F^2 + \frac{1}{2}\left\|\mathbf{\Lambda}_{\mathrm{M}}^{-\frac{1}{2}}\left(\mathbf{Y}_{\mathrm{M}} - \mathbf{RMA}\right)\right\|_F^2$$

and

$$\iota_{\mathcal{A}}(\mathbf{V}) = \begin{cases} 0 & \text{if } \mathbf{V} \in \mathcal{A} \\ +\infty & \text{otherwise.} \end{cases}$$

Recall that $\mathcal{A} = \left\{\mathbf{A} | \mathbf{A} \geq 0, \mathbf{1}_p^T\mathbf{A} = \mathbf{1}_n\right\}$.

The augmented Lagrangian associated with the optimization of $\mathbf{A}$ can be written as

$$\mathcal{L}(\mathbf{A}, \mathbf{V}, \mathbf{G}) = \frac{1}{2}\left\|\mathbf{\Lambda}_{\mathrm{H}}^{-\frac{1}{2}}\left(\mathbf{Y}_{\mathrm{H}} - \mathbf{MABS}\right)\right\|_F^2 + \iota_{\mathcal{A}}(\mathbf{V}) + \frac{1}{2}\left\|\mathbf{\Lambda}_{\mathrm{M}}^{-\frac{1}{2}}\left(\mathbf{Y}_{\mathrm{M}} - \mathbf{RMA}\right)\right\|_F^2 + \frac{\mu}{2}\left\|\mathbf{A} - \mathbf{V} - \mathbf{G}\right\|_F^2 \tag{12}$$

where $\mathbf{G}$ is the so-called scaled dual variable and $\mu > 0$ is the augmented Lagrange multiplier, weighting the augmented Lagrangian term [49]. The ADMM summarized in Algorithm 2, consists of an $\mathbf{A}$-minimization step, a $\mathbf{V}$-minimization step and a dual variable $\mathbf{G}$ update step (see [49] for further details about ADMM). Note that the operator $\Pi_{\mathcal{X}}(\mathbf{X})$ in Algorithm 2 represents projecting the variable $\mathbf{X}$ onto a set $\mathcal{X}$, which is defined as

$$\Pi_{\mathcal{X}}(\mathbf{X}) = \arg\min_{\mathbf{Z}\in\mathcal{X}} \left\|\mathbf{Z} - \mathbf{X}\right\|_F^2.$$

Algorithm 2: ADMM sub-iterations to estimate $\mathbf{A}$

Input: $\mathbf{Y}_{\mathrm{M}}$, $\mathbf{Y}_{\mathrm{H}}$, $\mathbf{\Lambda}_{\mathrm{M}}$, $\mathbf{\Lambda}_{\mathrm{H}}$, $\mathbf{R}$, $\mathbf{B}$, $\mathbf{S}$, $\mu > 0$

Initialization: $\mathbf{V}^{(0)}$,$\mathbf{G}^{(0)}$;

for $k = 0$ **to** *stopping rule* **do**

  /* Optimize w.r.t $\mathbf{A}$ (Algorithm 3) */

  $\mathbf{A}^{(t,k+1)} \in \arg\min_{\mathbf{A}} \mathcal{L}(\mathbf{A}, \mathbf{V}^{(k)}, \mathbf{G}^{(k)})$;

  /* Optimize w.r.t $\mathbf{V}$ (Algorithm 4) */

  $\mathbf{V}^{(k+1)} \leftarrow \Pi_{\mathcal{A}}(\mathbf{A}^{(t,k+1)} - \mathbf{G}^{(k)})$;

  /* Update Dual Variable $\mathbf{G}$ */

  $\mathbf{G}^{(k+1)} \leftarrow \mathbf{G}^{(k)} - \left(\mathbf{A}^{(t,k+1)} - \mathbf{V}^{(k+1)}\right)$;

end

Set $\mathbf{A}^{(t+1)} = \mathbf{A}^{(t,k+1)}$;

Output: $\mathbf{A}^{(t+1)}$

Given that the functions $L_1(\mathbf{A})$ and $\iota_{\mathcal{A}}(\mathbf{V})$ are both closed, proper, and convex, thus, invoking the Eckstein and Bertsekas theorem [50, Theorem 8], the convergence of Algorithm 2 to a solution of (11) is guaranteed.

1) Updating $\mathbf{A}$*:* In order to minimize (12) w.r.t. $\mathbf{A}$, we solve the equation $\partial\mathcal{L}(\mathbf{A}, \mathbf{V}^{(k)}, \mathbf{G}^{(k)})/\partial\mathbf{A} = \mathbf{0}$, which is equivalent to the generalized Sylvester equation

$$\mathbf{C}_1\mathbf{A} + \mathbf{A}\mathbf{C}_2 = \mathbf{C}_3 \tag{13}$$

where

$$\begin{aligned}
\mathbf{C}_1 &= \left(\mathbf{M}^T\mathbf{\Lambda}_{\mathrm{H}}^{-1}\mathbf{M}\right)^{-1}\left((\mathbf{RM})^T\mathbf{\Lambda}_{\mathrm{M}}^{-1}\mathbf{RM} + \mu\mathbf{I}_p\right) \\
\mathbf{C}_2 &= \mathbf{BS}\left(\mathbf{BS}\right)^T \\
\mathbf{C}_3 &= \left(\mathbf{M}^T\mathbf{\Lambda}_{\mathrm{H}}^{-1}\mathbf{M}\right)^{-1}\left(\mathbf{M}^T\mathbf{\Lambda}_{\mathrm{H}}^{-1}\mathbf{Y}_{\mathrm{H}}\left(\mathbf{BS}\right)^T\right. \\
&\quad \left. + (\mathbf{RM})^T\mathbf{\Lambda}_{\mathrm{M}}^{-1}\mathbf{Y}_{\mathrm{M}} + \mu(\mathbf{V}^{(k)} + \mathbf{G}^{(k)})\right).
\end{aligned}$$

Eq. (13) can be solved analytically by exploiting the properties of the circulant and downsampling matrices $\mathbf{B}$ and $\mathbf{S}$, as summarized in Algorithm 3 and demonstrated in [46]. Note that the matrix $\mathbf{F}$ represents the FFT operation and its conjugate transpose (or Hermitian transpose) $\mathbf{F}^H$ represents the iFFT operation. The matrix $\mathbf{D} \in \mathbb{C}^{n\times n}$ is a diagonal matrix, which

has eigenvalues of the matrix $\mathbf{B}$ in its diagonal line and can be rewritten as

$$\mathbf{D} = \begin{bmatrix} \mathbf{D}_1 & \mathbf{0} & \cdots & \mathbf{0} \\ \mathbf{0} & \mathbf{D}_2 & \cdots & \mathbf{0} \\ \vdots & \vdots & \ddots & \vdots \\ \mathbf{0} & \mathbf{0} & \cdots & \mathbf{D}_d \end{bmatrix}$$

where $\mathbf{D}_i \in \mathbb{C}^{m\times m}$. Thus, we have $\bar{\mathbf{D}}^H\bar{\mathbf{D}} = \sum_{t=1}^{d}\mathbf{D}_t^H\mathbf{D}_t = \sum_{t=1}^{d}\mathbf{D}_t^2$, where $\bar{\mathbf{D}} = \mathbf{D}\left(\mathbf{1}_d \otimes \mathbf{I}_m\right)$. Similarly, the diagonal matrix $\mathbf{\Lambda_C}$ has eigenvalues of the matrix $\mathbf{C}_1$ in its diagonal line (denoted as $\lambda_1, \cdots, \lambda_{\widetilde{m}_\lambda}$ and $\lambda_i \geq 0$, $\forall i$). The matrix $\mathbf{Q}$ contains eigenvectors of the matrix $\mathbf{C}_1$ in its columns. The auxiliary matrix $\bar{\mathbf{A}} \in \mathbb{C}^{m_\lambda \times n}$ is decomposed as $\bar{\mathbf{A}} = \left[\bar{\boldsymbol{a}}_1^T, \bar{\boldsymbol{a}}_2^T, \cdots, \bar{\boldsymbol{a}}_p^T\right]^T$.

Algorithm 3: A closed-form solution of (13) w.r.t. $\mathbf{A}$

Input: $\mathbf{Y}_\mathrm{M}$, $\mathbf{Y}_\mathrm{H}$, $\mathbf{\Lambda}_\mathrm{M}$, $\mathbf{\Lambda}_\mathrm{H}$, $\mathbf{R}$, $\mathbf{B}$, $\mathbf{S}$, $\mathbf{V}^{(k)}$, $\mathbf{G}^{(k)}$, $\mu > 0$

/* Circulant matrix decomposition: $\mathbf{B} = \mathbf{F}\mathbf{D}\mathbf{F}^H$ */

$\mathbf{D} \leftarrow \mathrm{EigDec}\left(\mathbf{B}\right)$;

$\bar{\mathbf{D}} \leftarrow \mathbf{D}\left(\mathbf{1}_d \otimes \mathbf{I}_m\right)$;

/* Calculate $\mathbf{C}_1$ */

$\mathbf{C}_1 \leftarrow \left(\mathbf{M}^T\mathbf{\Lambda}_\mathrm{H}^{-1}\mathbf{M}\right)^{-1}\left((\mathbf{R}\mathbf{M})^T\mathbf{\Lambda}_\mathrm{M}^{-1}\mathbf{R}\mathbf{M} + \mu\mathbf{I}_p\right)$;

/* Eigen-decomposition of $\mathbf{C}_1$: $\mathbf{C}_1 = \mathbf{Q}\mathbf{\Lambda}_C\mathbf{Q}^{-1}$ */

$(\mathbf{Q}, \mathbf{\Lambda}_C) \leftarrow \mathrm{EigDec}\left(\mathbf{C}_1\right)$;

/* Calculate $\mathbf{C}_3$ */

$\mathbf{C}_3 \leftarrow \left(\mathbf{M}^T\mathbf{\Lambda}_\mathrm{H}^{-1}\mathbf{M}\right)^{-1}\left(\mathbf{M}^T\mathbf{\Lambda}_\mathrm{H}^{-1}\mathbf{Y}_\mathrm{H}\left(\mathbf{B}\mathbf{S}\right)^T + (\mathbf{R}\mathbf{M})^T\mathbf{\Lambda}_\mathrm{M}^{-1}\mathbf{Y}_\mathrm{M} + \mu(\mathbf{V}^{(k)} + \mathbf{G}^{(k)})\right)$;

/* Calculate $\bar{\mathbf{C}}_3$ */

$\bar{\mathbf{C}}_3 \leftarrow \mathbf{Q}^{-1}\mathbf{C}_3\mathbf{F}$;

/* Calculate $\bar{\mathbf{A}}$ band by band */

for $l = 1$ **to** p **do**

  /* Calculate the lth band */

  $\bar{\boldsymbol{a}}_l \leftarrow \lambda_l^{-1}(\bar{\mathbf{C}}_3)_l - \lambda_l^{-1}(\bar{\mathbf{C}}_3)_l\bar{\mathbf{D}}\left(\lambda_l d\mathbf{I}_m + \sum_{t=1}^{d}\mathbf{D}_t^2\right)\bar{\mathbf{D}}^H$;

end

Set $\mathbf{A} = \mathbf{Q}\bar{\mathbf{A}}\mathbf{F}^H$;

Output: $\mathbf{A}$

2) Updating $\mathbf{V}$*:* The update of $\mathbf{V}$ can be made by simply computing the Euclidean projection of $\mathbf{A}^{(t,k+1)} - \mathbf{G}^{(k+1)}$ onto the canonical simplex $\mathcal{A}$, which can be expressed as follows

$$\begin{aligned}\hat{\mathbf{V}} &= \arg\min_{\mathbf{V}} \frac{\mu}{2}\left\|\mathbf{V} - \left(\mathbf{A}^{(t,k+1)} - \mathbf{G}^{(k+1)}\right)\right\|_F^2 + \iota_{\mathcal{A}}(\mathbf{V}) \\ &= \Pi_{\mathcal{A}}\left(\mathbf{A}^{(t,k+1)} - \mathbf{G}^{(k+1)}\right)\end{aligned}$$

where $\Pi_{\mathcal{A}}$ denotes the projection (in the sense of the Euclidean norm) onto the simplex $\mathcal{A}$. This classical projection problem has been widely studied and can be achieved by numerous methods [51]–[54]. In this work, we adopt the popular strategy first proposed in [51] and summarized in Algorithm 4. Note that the above optimization is decoupled w.r.t. the columns of $\mathbf{V}$, denoted by $(\mathbf{V})_1, \cdots, (\mathbf{V})_n$, which accelerates the projection dramatically.

Algorithm 4: Projection onto the Simplex $\mathcal{A}$

Input: $\mathbf{A}^{(t,k+1)} - \mathbf{G}^{(k)}$

for $i = 1$ **to** n **do**

  $(\mathbf{A} - \mathbf{G})_i \triangleq i^{\text{th}}$ column of $\mathbf{A}^{(t,k+1)} - \mathbf{G}^{(k)}$;

  /* Sorting the elements of $(\mathbf{A} - \mathbf{G})_i$ */

  Sort $(\mathbf{A} - \mathbf{G})_i$ into $\mathbf{y}$: $y_1 \geq \cdots \geq y_p$;

  Set $K := \max_{1\leq k\leq p}\{k | \left(\sum_{r=1}^{k} y_r - 1\right)/k < y_k\}$;

  Set $\tau := \left(\sum_{r=1}^{K} y_r - 1\right)/K$;

  /* The max operation is component-wise */

  Set $(\hat{\mathbf{V}})_i := \max\{(\mathbf{A} - \mathbf{G})_i - \tau, 0\}$;

end

Output: $\mathbf{V}^{(k+1)} = \hat{\mathbf{V}}$

In practice, the ASC constraint is sometimes criticized for not being able to account for every material in a pixel or due to endmember variability [27]. In this case, the sum-to-one constraint can be simply removed. Thus, the Algorithm 4 will degenerate to projecting $(\mathbf{A} - \mathbf{G})_i$ onto the non-negative half-space, which simply consists of setting the negative values of $(\mathbf{A} - \mathbf{G})_i$ to zeros.

C. Optimization w.r.t. the Endmember Matrix $\mathbf{M}$ ($\mathbf{A}$ fixed)

The minimization of (10) w.r.t. the abundance matrix $\mathbf{M}$ conditional on $\mathbf{A}$ can be formulated as

$$\min_{\mathbf{M}} \quad L_1(\mathbf{M}) + \iota_{\mathcal{M}}(\mathbf{M}) \tag{14}$$

where $L_1(\mathbf{M}) =$

$$\frac{1}{2}\left\|\mathbf{\Lambda}_\mathrm{H}^{-\frac{1}{2}}\left(\mathbf{Y}_\mathrm{H} - \mathbf{M}\mathbf{A}_\mathrm{H}\right)\right\|_F^2 + \frac{1}{2}\left\|\mathbf{\Lambda}_\mathrm{M}^{-\frac{1}{2}}\left(\mathbf{Y}_\mathrm{M} - \mathbf{R}\mathbf{M}\mathbf{A}\right)\right\|_F^2$$

and $\mathbf{A}_\mathrm{H} = \mathbf{A}\mathbf{B}\mathbf{S}$. By splitting the quadratic data fidelity term and the inequality constraints, the augmented Lagrangian for (15) can be expressed as

$$\mathcal{L}(\mathbf{M}, \mathbf{T}, \mathbf{G}) = L_1(\mathbf{M}) + \iota_{\mathcal{M}}(\mathbf{\Lambda}_\mathrm{H}^{\frac{1}{2}}\mathbf{T}) + \frac{\mu}{2}\left\|\mathbf{\Lambda}_\mathrm{H}^{-\frac{1}{2}}\mathbf{M} - \mathbf{T} - \mathbf{G}\right\|_F^2. \tag{15}$$

The optimization of $\mathcal{L}(\mathbf{M}, \mathbf{T}, \mathbf{G})$ consists of updating $\mathbf{M}$, $\mathbf{T}$ and $\mathbf{G}$ iteratively as summarized in Algorithm 5 and detailed below. As $L_1(\mathbf{M})$ and $\iota_{\mathcal{M}}(\mathbf{\Lambda}_\mathrm{H}^{\frac{1}{2}}\mathbf{T})$ are closed, proper and convex functions and $\mathbf{\Lambda}_\mathrm{H}^{\frac{1}{2}}$ has full column rank, the ADMM is guaranteed to converge to a solution of problem (14).

1) Updating $\mathbf{M}$*:* Forcing the derivative of (15) w.r.t. $\mathbf{M}$ to be zero leads to the following Sylvester equation

$$\mathbf{H}_1\mathbf{M} + \mathbf{M}\mathbf{H}_2 = \mathbf{H}_3 \tag{16}$$

Algorithm 5: ADMM sub-iterations to estimate $\mathbf{M}$

Input: $\mathbf{Y}_{\mathrm{M}}$, $\mathbf{Y}_{\mathrm{H}}$, $\mathbf{\Lambda}_{\mathrm{M}}$, $\mathbf{\Lambda}_{\mathrm{H}}$, $\mathbf{R}$, $\mathbf{B}$, $\mathbf{S}$, $\mathbf{A}$, $\mu > 0$

Initialization: $\mathbf{T}^{(0)}$,$\mathbf{G}^{(0)}$;

for $k = 0$ **to** *stopping rule* **do**

/* Optimize w.r.t $\mathbf{M}$ */

$\mathbf{M}^{(t,k+1)} \in \arg\min_{\mathbf{M}} \mathcal{L}(\mathbf{M}, \mathbf{T}^{(k)}, \mathbf{G}^{(k)})$;

/* Optimize w.r.t $\mathbf{T}$ */

$\mathbf{T}^{(k+1)} \leftarrow \Pi_{\mathcal{T}}(\mathbf{\Lambda}_{\mathrm{H}}^{-\frac{1}{2}}\mathbf{M}^{(t,k+1)} - \mathbf{G}^{(k)})$;

/* Update Dual Variable $\mathbf{G}$ */

$\mathbf{G}^{(k+1)} \leftarrow \mathbf{G}^{(k)} - \left(\mathbf{\Lambda}_{\mathrm{H}}^{-\frac{1}{2}}\mathbf{M}^{(k+1)} - \mathbf{T}^{(k+1)}\right)$;

end

Set $\mathbf{M}^{(t+1)} = \mathbf{M}^{(t,k+1)}$;

Output: $\mathbf{M}^{(t+1)}$

where

$$\mathbf{H}_1 = \mathbf{\Lambda}_{\mathrm{H}}\mathbf{R}^T\mathbf{\Lambda}_{\mathrm{M}}^{-1}\mathbf{R}$$

$$\mathbf{H}_2 = \left(\mathbf{A}_{\mathrm{H}}\mathbf{A}_{\mathrm{H}}{}^T + \mu\mathbf{I}_p\right)\left(\mathbf{A}\mathbf{A}^T\right)^{-1}$$

$$\mathbf{H}_3 = \left[\mathbf{Y}_{\mathrm{H}}\mathbf{A}_{\mathrm{H}}^T + \mathbf{\Lambda}_{\mathrm{H}}\mathbf{R}^T\mathbf{\Lambda}_{\mathrm{M}}^{-1}\mathbf{Y}_{\mathrm{M}}\mathbf{A}^T + \mu\mathbf{\Lambda}_{\mathrm{H}}^{\frac{1}{2}}(\mathbf{T}+\mathbf{G})\right]\left(\mathbf{A}\mathbf{A}^T\right)^{-1}$$

Note that $\mathrm{vec}(\mathbf{AXB}) = \left(\mathbf{B}^T \otimes \mathbf{A}\right)\mathrm{vec}(\mathbf{X})$, where $\mathrm{vec}\,(\mathbf{X})$ denotes the vectorization of the matrix $\mathbf{X}$ formed by stacking the columns of $\mathbf{X}$ into a single column vector and $\otimes$ denotes the Kronecker product [55]. Thus, vectorizing both sides of (16) leads to[2]

$$\mathbf{W}\mathrm{vec}(\mathbf{M}) = \mathrm{vec}(\mathbf{H}_3) \tag{17}$$

where $\mathbf{W} = \left(\mathbf{I}_p \otimes \mathbf{H}_1 + \mathbf{H}_2^T \otimes \mathbf{I}_{m_\lambda}\right)$. Thus, $\mathrm{vec}\left(\hat{\mathbf{M}}\right) = \mathbf{W}^{-1}\mathrm{vec}(\mathbf{H}_3)$. Note that $\mathbf{W}^{-1}$ can be computed and stored in advance instead of being computed in each iteration.

Alternatively, there exists a more efficient way to calculate the solution $\mathbf{M}$ analytically (avoiding to compute the inverse of the matrix $\mathbf{W}$). Note that the matrices $\mathbf{H}_1 \in \mathbb{R}^{m_\lambda \times m_\lambda}$ and $\mathbf{H}_2 \in \mathbb{R}^{p \times p}$ are both the products of two symmetric positive definite matrices. According to the Lemma 1 in [56], $\mathbf{H}_1$ and $\mathbf{H}_2$ can be diagonalized by eigen-decomposition, i.e., $\mathbf{H}_1 = \mathbf{V}_1\mathbf{O}_1\mathbf{V}_1^{-1}$ and $\mathbf{H}_2 = \mathbf{V}_2\mathbf{O}_2\mathbf{V}_2^{-1}$, where $\mathbf{O}_1$ and $\mathbf{O}_2$ are diagonal matrices denoted as

$$\begin{aligned}\mathbf{O}_1 &= \mathrm{diag}\{s_1, \cdots, s_{m_\lambda}\} \\ \mathbf{O}_2 &= \mathrm{diag}\{t_1, \cdots, t_p\}.\end{aligned} \tag{18}$$

Thus, (16) can be transformed to

$$\mathbf{O}_1\tilde{\mathbf{M}} + \tilde{\mathbf{M}}\mathbf{O}_2 = \mathbf{V}_1^{-1}\mathbf{H}_3\mathbf{V}_2. \tag{19}$$

where $\tilde{\mathbf{M}} = \mathbf{V}_1^{-1}\mathbf{M}\mathbf{V}_2$. Straightforward computations lead to

$$\tilde{\mathbf{H}} \circ \tilde{\mathbf{M}} = \mathbf{V}_1^{-1}\mathbf{H}_3\mathbf{V}_2 \tag{20}$$

where

$$\tilde{\mathbf{H}} = \begin{bmatrix} s_1+t_1 & s_1+t_2 & \cdots & s_1+t_p \\ s_2+t_1 & s_2+t_2 & \cdots & s_2+t_p \\ \vdots & \vdots & \ddots & \vdots \\ s_{m_\lambda}+t_1 & s_{m_\lambda}+t_2 & \cdots & s_{m_\lambda}+t_p \end{bmatrix} \tag{21}$$

and $\circ$ represents the Hadamard product, defined as the component-wise product of two matrices (having the same size). Then, $\tilde{\mathbf{M}}$ can be calculated by component-wise division of $\mathbf{V}_1^{-1}\mathbf{H}_3\mathbf{V}_2$ and $\tilde{\mathbf{H}}$. Finally, $\mathbf{M}$ can be estimated as $\hat{\mathbf{M}} = \mathbf{V}_1\tilde{\mathbf{M}}\mathbf{V}_2^{-1}$. Note that the computational complexity of the latter strategy is of order $\mathcal{O}(\max(m_\lambda^3, p^3))$, which is lower than the complexity order $\mathcal{O}((m_\lambda p)^3))$ of solving (17).

2) Updating $\mathbf{T}$*:* The optimization w.r.t. $\mathbf{T}$ can be transformed as

$$\arg\min_{\mathbf{T}} \frac{1}{2}\left\|\mathbf{T} - \mathbf{\Lambda}_{\mathrm{H}}^{-\frac{1}{2}}\mathbf{M} + \mathbf{G}\right\| + \iota_{\mathcal{T}}(\mathbf{T}) \tag{22}$$

where $\iota_{\mathcal{T}}(\mathbf{T}) = \iota_{\mathcal{M}}(\mathbf{\Lambda}_{\mathrm{H}}^{\frac{1}{2}}\mathbf{T})$. As $\mathbf{\Lambda}_{\mathrm{H}}^{-\frac{1}{2}}$ is a diagonal matrix, the solution of (22) can be obtained easily by setting

$$\hat{\mathbf{T}} = \mathbf{\Lambda}_{\mathrm{H}}^{-\frac{1}{2}}\min\left(\max\left(\mathbf{M} - \mathbf{\Lambda}_{\mathrm{H}}^{\frac{1}{2}}\mathbf{G}, 0\right), 1\right) \tag{23}$$

where min and max are to be understood component-wise.

Remark. *If the endmember signatures are fixed a priori, i.e.,* $\mathbf{M}$ *is known, the unsupervised unmixing and fusion will degenerate to a supervised unmixing and fusion by simply not updating* $\mathbf{M}$*. In this case, the alternating scheme is not necessary, since Algorithm 1 reduces to Algorithm 2. Note that fixing* $\mathbf{M}$ *a priori transforms the non-convex problem* (10) *into a convex one, which can be solved much more efficiently. The solution produced by the resulting algorithm is also guaranteed to be the global optimal point instead of a stationary point.*

D. Parallelization

We remark that some of the most computationally intensive steps of the proposed algorithm can be easily parallelized on a parallel computation platform. More specifically, the estimation of $\mathbf{A}$ in Algorithm 3 can be parallelized in frequency domain due to the structure of blurring and downsampling matrices in spectral domain. Projection onto the simplex $\mathcal{A}$ can also be parallelized.

E. Relation with some similar algorithms

At this point, we remark that there exist a number of joint fusion and unmixing algorithms which exhibit some similarity with ours, namely the methods in [15], [19], [26][3]. Next, we state differences between those methods and ours. First of all, the degradation model used in [19] follows the pixel aggregation assumption. This assumption makes a block-by-block inversion possible (see equation (18) in [19]), which significantly reduces the computational complexity. However, due to the convolution (matrix $\mathbf{B}$ in (2)) plus downsampling

[2]The vectorization of the matrics $\mathbf{M}$,$\mathbf{H}_1$ and $\mathbf{H}_2$ is easy to do as the size of these matrices are small, which is not true for the matrices $\mathbf{A}$, $\mathbf{C}_1$ and $\mathbf{C}_2$ in (13).

[3]Note that some other fusion techniques (e.g., [12], [56], [57]), which only deal with the fusion problem and do not consider the unmixing constraints, are not considered in this work.

(matrix $\mathbf{S}$ in (2)) model used in our work, this simplification no longer applies. Works [15], [26] use a degradation model and an optimization formulation similar to ours. The main difference is that both works [15], [26] minimize an approximate objective function to bypass the difficulty arising from the entanglement of spectral and spatial information contained in HS and MS images. More specifically, both works minimize only the HS data term and ignore the MS one when updating the endmembers and minimize only MS data term and ignore the HS one when updating the abundances. On the contrary, in the proposed method, the exact objective function is minimized directly thanks to the available Sylvester equation solvers. Thus, both HS and MS images contribute to the estimation of endmembers and abundances.

V. Experimental results

This section applies the proposed unmixing based fusion method to multi-band images associated with both synthetic and semi-real data. All the algorithms have been implemented using MATLAB R2014A on a computer with Intel(R) Core(TM) i7-2600 CPU@3.40GHz and 8GB RAM. The MATLAB codes and all the simulation results are available in the first author's homepage[4].

A. Quality metrics

1) Fusion quality: To evaluate the quality of the fused image, we use the reconstruction signal-to-noise ratio (RSNR), the averaged spectral angle mapper (SAM), the universal image quality index (UIQI), the relative dimensionless global error in synthesis (ERGAS) and the degree of distortion (DD) as quantitative measures.

a) RSNR: The reconstruction signal-to-noise ratio (RSNR) is defined as

$$\text{RSNR}(\mathbf{X}, \hat{\mathbf{X}}) = 10 \log_{10} \left(\frac{\|\mathbf{X}|_F^2}{\|\mathbf{X} - \hat{\mathbf{X}}\|_F^2} \right)$$

where $\mathbf{X}$ and $\hat{\mathbf{X}}$ denote, respectively, the actual image and fused image. The larger RSNR, the better the fusion quality.

b) SAM: The spectral angle mapper (SAM) measures the spectral distortion between the actual and fused images. The SAM of two spectral vectors $\boldsymbol{x}_n$ and $\hat{\boldsymbol{x}}_n$ is defined as

$$\text{SAM}(\boldsymbol{x}_n, \hat{\boldsymbol{x}}_n) = \arccos \left(\frac{\langle \boldsymbol{x}_n, \hat{\boldsymbol{x}}_n \rangle}{\|\boldsymbol{x}_n\|_2 \|\hat{\boldsymbol{x}}_n\|_2} \right).$$

The overall SAM is obtained by averaging the SAMs computed from all image pixels. Note that the value of SAM is expressed in degrees and thus belongs to $[0, 180[$. The smaller the value of SAM, the less the spectral distortion.

c) UIQI: The universal image quality index (UIQI) is related to the correlation, luminance distortion, and contrast distortion of the estimated image w.r.t. the reference image. The UIQI between two single-band images $\mathbf{x} = [x_1, x_2, \ldots, x_N]$ and $\hat{\mathbf{x}} = [\hat{x}_1, \hat{x}_2, \ldots, \hat{x}_N]$ is defined as

$$\text{UIQI}(\mathbf{x}, \hat{\mathbf{x}}) = \frac{4\sigma_{x\hat{x}}^2 \mu_x \mu_{\hat{x}}}{(\sigma_x^2 + \sigma_{\hat{x}}^2)(\mu_x^2 + \mu_{\hat{x}}^2)}$$

where $\left(\mu_x, \mu_{\hat{x}}, \sigma_x^2, \sigma_{\hat{x}}^2\right)$ are the sample means and variances of x and $\hat{x}$, and $\sigma_{x\hat{x}}^2$ is the sample covariance of $(x, \hat{x})$. The range of UIQI is $[-1, 1]$ and $\text{UIQI}(\mathbf{x}, \hat{\mathbf{x}}) = 1$ when $\mathbf{x} = \hat{\mathbf{x}}$. For multi-band images, the overall UIQI can be computed by averaging the UIQI computed band-by-band.

d) ERGAS: The relative dimensionless global error in synthesis (ERGAS) calculates the amount of spectral distortion in the image. This measure of fusion quality is defined as

$$\text{ERGAS} = 100 \times \frac{m}{n} \sqrt{\frac{1}{m_\lambda} \sum_{i=1}^{m_\lambda} \left(\frac{\text{RMSE}(i)}{\mu_i} \right)^2}$$

where m/n is the ratio between the pixel sizes of the MS and HS images, μ_i is the mean of the ith band of the HS image, and m_λ is the number of HS bands. The smaller ERGAS, the smaller the spectral distortion.

e) DD: The degree of distortion (DD) between two images $\mathbf{X}$ and $\hat{\mathbf{X}}$ is defined as

$$\text{DD}(\mathbf{X}, \hat{\mathbf{X}}) = \frac{1}{n m_\lambda} \|\text{vec}(\mathbf{X}) - \text{vec}(\hat{\mathbf{X}})\|_1$$

where vec represents the vectorization and $\|\cdot\|_1$ represents the ℓ_1 norm. The smaller DD, the better the fusion.

2) Unmixing quality: In order to analyze the quality of the unmixing results, we consider the normalized mean square error (NMSE) for both endmember and abundance matrices

$$\text{NMSE}_{\mathbf{M}} = \frac{\|\widehat{\mathbf{M}} - \mathbf{M}\|_F^2}{\|\mathbf{M}\|_F^2}$$

$$\text{NMSE}_{\mathbf{A}} = \frac{\|\widehat{\mathbf{A}} - \mathbf{A}\|_F^2}{\|\mathbf{A}\|_F^2}.$$

The smaller NMSE, the better the quality of the unmixing. The SAM between the actual and estimated endmembers (different from SAM defined previously for pixel vectors) is a measure of spectral distortion defined as

$$\text{SAM}_{\mathbf{M}}(\boldsymbol{m}_n, \hat{\boldsymbol{m}}_n) = \arccos \left(\frac{\langle \boldsymbol{m}_n, \hat{\boldsymbol{m}}_n \rangle}{\|\boldsymbol{m}_n\|_2 \|\hat{\boldsymbol{m}}_n\|_2} \right).$$

The overall SAM is finally obtained by averaging the SAMs computed from all endmembers.

B. Synthetic data

This section applies the proposed FUMI method to synthetic data and compares it with the joint unmixing and fusion methods investigated in [22], [15] and [26].

To simulate high-resolution HS images, natural spatial patterns have been used for abundance distributions as in [58]. There is one vector of abundance per pixel, i.e., $\mathbf{A} \in \mathbb{R}^{p \times 100^2}$, for the considered image of size 100×100 pixels in [58]. The reference endmembers, shown in Fig. 1, are m reflectance spectra selected randomly from the United States Geological Survey (USGS) digital spectral library[5]. Each reflectance spectrum consists of $L = 221$ spectral bands from 400 nm to 2508 nm. In this simulation, the number of endmembers is fixed to $p = 9$. The synthetic image is then generated by the product of endmembers and abundances, i.e., $\mathbf{X} = \mathbf{MA}$. Considering the

[4] http://sigproc.eng.cam.ac.uk/Main/QW245/

[5] http://speclab.cr.usgs.gov/spectral.lib06/

different distributions of abundances, five patterns in [58] have been used as the ground-truth abundances and all the results in the following sections have been obtained by averaging these five patterns results.

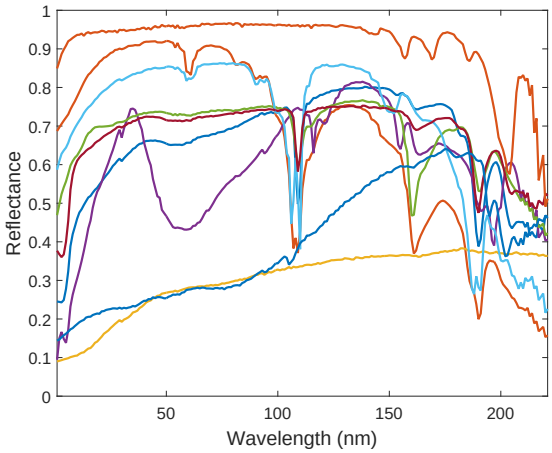

Fig. 1: Endmember signatures for synthetic data.

1) HS and MS image fusion: In this section, we consider the fusion of HS and MS images. The HS image $\mathbf{Y}_{\mathrm{H}}$ has been generated by applying a 11×11 Gaussian filter (with zero mean and standard deviation $\sigma_{\mathbf{B}} = 1.7$) and then by down-sampling every 4 pixels in both vertical and horizontal directions for each band of the reference image. A 4-band MS image $\mathbf{Y}_{\mathrm{M}}$ has been obtained by filtering $\mathbf{X}$ with the LANDSAT-like reflectance spectral responses. The HS and MS images are both contaminated by zero-mean additive Gaussian noises. Considering that the methods in [22], [15] and [26] did not consider weighting the cost function with the noise covariance knowledge, we have added noise with identical power to all HS and MS bands to guarantee a fair comparison. The power of the noise s^2 is set to SNR $= 40$dB, where $\mathrm{SNR} = 10\log\left(\frac{\|\mathbf{XBS}\|_F^2}{m_\lambda m s^2}\right)$.

Before comparing different methods, several implementation issues are explained in the following.

- **Initialization**: As shown in Algorithm 1, the proposed algorithm only requires the initialization of the endmember matrix $\mathbf{M}$. Theoretically, any endmember extraction algorithm (EEA) can be used to initialize $\mathbf{M}$. In this work, we have used the *vertex component analysis* (VCA) method [39], which is a state-of-the-art method that does not require the presence of pure pixels in the image.
- **Subspace Identification**: For the endmember estimation, a popular strategy is to use a subspace transformation as a preprocessing step, such as in [40], [48]. In general, the subspace transformation is estimated *a priori* from the high-spectral resolution image, e.g., from the HS data. In this work, the projection matrix denoted as $\mathbf{E}$ has been learned by computing the singular value decomposition (SVD) of $\mathbf{Y}_{\mathrm{H}}$ and retaining the left-singular vectors associated with the largest eigenvalues. Then the input HS data $\mathbf{Y}_{\mathrm{H}}$, the HS noise covariance matrix $\mathbf{\Lambda}_{\mathrm{H}}$ and the spectral response $\mathbf{R}$ in Algorithm 1 are replaced with their projections onto the learned subspace as $\mathbf{Y}_{\mathrm{H}} \leftarrow \mathbf{E}^T\mathbf{Y}_{\mathrm{H}}$, $\mathbf{\Lambda}_{\mathrm{H}} \leftarrow \mathbf{E}^T\mathbf{\Lambda}_{\mathrm{H}}\mathbf{E}$ and $\mathbf{R} \leftarrow \mathbf{RE}$, where $\mathbf{E} \in \mathbf{R}^{m_\lambda \times \widetilde{m}_\lambda}$ is the estimated orthogonal basis using SVD and $\widetilde{m}_\lambda \ll m_\lambda$. Given that the formulation using the transformed entities is equivalent to the original one but the matrix dimension is now much smaller, the subspace transformation brings huge numerical advantage.
- **Parameters in ADMM**: The value of μ adopted in all the experiments is fixed to the average of the noise power of HS and MS images, which is motivated by balancing the data term and regularization term. As ADMM is used to solve sub-problems, it is not necessary to use complicated stopping rule to run ADMM exhaustively. Thus, the number of ADMM iterations has been fixed to 30. Experiments have demonstrated that varying these parameters do not affect much the convergence of the whole algorithm.
- **Stopping rule**: The stopping rule for Algorithm 1 is that the relative difference for the successive updates of the objective $L(\mathbf{M}, \mathbf{A})$ is less than 10^{-4}, i.e.,

$$\frac{|L(\mathbf{M}^{(t+1)}, \mathbf{A}^{(t+1)}) - L(\mathbf{M}^{(t)}, \mathbf{A}^{(t)})|}{|L(\mathbf{M}^{(t)}, \mathbf{A}^{(t)})|} \leq 10^{-4}.$$

- **Parameter setting for compared algorithms**: The original implementation of three state-of-the-art methods in [22], [15] and [26] was used as baseline. The respective parameters were tuned for best performance. For all the algorithms, we use the same initial endmembers and abundances. For [22] and [15], the threshold for the convergence condition of NMF was set at 10^{-4} as the authors suggested.

The fusion and unmixing results using different methods are reported in Tables II and III, respectively. Both matrices $\mathbf{A}$ and $\mathbf{M}$ have been estimated. For fusion performance, the proposed FUMI method outperforms the other three methods, with a price of high time complexity. Berne's method uses the least CPU time. Regarding unmixing, Lanaras's method and FUMI perform similarly and are both much better than the other two methods.

TABLE III: Unmixing Performance for Synthetic HS+MS dataset: $\mathrm{SAM}_{\mathbf{M}}$ (in degree), $\mathrm{NMSE}_{\mathbf{M}}$ (in dB) and $\mathrm{NMSE}_{\mathbf{A}}$ (in dB).

Methods	$\mathrm{SAM}_{\mathbf{M}}$	$\mathrm{NMSE}_{\mathbf{M}}$	$\mathrm{NMSE}_{\mathbf{A}}$
Berne [22]	3.27±1.44	-20.44±2.33	-6.07±1.96
Yokoya [15]	4.31±1.65	-19.32±2.67	-5.61±1.34
Lanaras [26]	**2.65±0.98**	**-23.01±3.08**	**-7.03±2.27**
FUMI	2.72±1.12	-22.50±2.34	-6.81±2.23

Robustness to endmember initialization: As the joint fusion and unmixing problem is non-convex, owing to the matrix factorization term, the initialization is crucial. An inappropriate initialization may induce a convergence to a point which is far from the desired endmembers and abundances. In order to illustrate this point, we have tested the proposed algorithm by initializing the endmembers $\mathbf{M}_0$ using different endmember extraction algorithms, e.g., N-FINDR [59], VCA [39] and SVMAX [60]. The fusion and unmixing results with

TABLE II: Fusion Performance for Synthetic HS+MS dataset: RSNR (in dB), UIQI, SAM (in degree), ERGAS, DD (in 10^{-2}) and time (in second).

Methods	RSNR	UIQI	SAM	ERGAS	DD	Time
Berne [22]	24.60±1.77	0.9160±0.0467	2.03±0.50	1.71±0.32	2.32±0.55	**8.04±0.72**
Yokoya [15]	27.26±0.88	0.9517±0.0220	1.63±0.20	1.24±0.10	1.79±0.25	13.04±0.86
Lanaras [26]	28.46±0.59	0.9625±0.0145	1.407±0.154	1.08±0.08	1.50±0.16	12.71±0.94
FUMI	**29.43±1.09**	**0.9710±0.0142**	**1.28±0.19**	**0.97±0.11**	**1.37±0.23**	21.90±3.32

TABLE IV: Fusion Performance of FUMI for one HS+MS dataset with different initializations: RSNR (in dB), UIQI, SAM (in degree), ERGAS and DD (in 10^{-2}) .

Initial	RSNR	UIQI	SAM	ERGAS	DD
VCA	30.68	0.9861	1.12	0.83	1.12
N-FINDR	30.94	0.9869	1.09	0.80	1.09
SVMAX	30.87	0.9866	1.09	0.81	1.09

these different initializations have been given in Tables IV and V. With these popular initialization methods, the fusion and unmixing performances are quite similar and show the robustness of the proposed method.

TABLE V: Unmixing Performance of FUMI for one HS+MS dataset with different initializations: $\text{SAM}_{\mathbf{M}}$ (in degree), $\text{NMSE}_{\mathbf{M}}$ (in dB) and $\text{NMSE}_{\mathbf{A}}$ (in dB).

Initial	$\text{SAM}_{\mathbf{M}}$	$\text{NMSE}_{\mathbf{M}}$	$\text{NMSE}_{\mathbf{A}}$
VCA	1.98	-23.96	-9.06
N-FINDR	1.72	-24.25	-9.31
SVMAX	1.72	-24.24	-9.28

2) HS and PAN image fusion: When the number of MS bands degrade to one, the fusion of HS and MS degenerates to HS pansharpening, which is a more challenging problem. In this experiment, the PAN image is obtained by averaging the first 50 bands of the reference image. The quantitative results for fusion and unmixing are summarized in Tables VI and VII, respectively. In terms of fusion performance, the proposed FUMI method outperforms the competitors for all the quality measures, using, however, the most CPU time, whereas Lanaras's uses the least. Regarding the unmixing performance, Lanaras's method and FUMI yield the best estimation result, outperforming the other two methods.

TABLE VII: Unmixing Performance for Synthetic HS+PAN dataset: $\text{SAM}_{\mathbf{M}}$ (in degree), $\text{NMSE}_{\mathbf{M}}$ (in dB) and $\text{NMSE}_{\mathbf{A}}$ (in dB).

Methods	$\text{SAM}_{\mathbf{M}}$	$\text{NMSE}_{\mathbf{M}}$	$\text{NMSE}_{\mathbf{A}}$
Berne [22]	3.27±1.44	-20.44±2.33	-5.24±1.87
Yokoya [15]	4.12±1.46	-19.69±2.80	-4.90±1.35
Lanaras [26]	**2.54±1.08**	**-22.69±2.58**	**-6.09±2.00**
FUMI	2.75±1.13	-21.94±2.17	-6.10±2.08

C. Semi-real data

In this section, we test the proposed FUMI algorithm on semi-real datasets, for which we have the real HS image as the reference image and have simulated the degraded images from the reference image.

In this experiment, the reference image is an HS image of size $200 \times 100 \times 176$ acquired over Moffett field, CA, in 1994 by the JPL/NASA airborne visible/infrared imaging spectrometer (AVIRIS) [61]. This image was initially composed of 224 bands that have been reduced to 176 bands after removing the water vapor absorption bands. A composite color image of the scene of interest is shown in the top right of Fig. 2. As there is no ground truth for endmembers and abundances for the reference image, we have first unmixed this image (with any unsupervised unmixing method) and then reconstructed the reference image $\mathbf{X}$ with the estimated endmembers and abundances (after appropriate normalization). The number of endmembers has been fixed to $p = 5$.

1) HS and MS image fusion: The observed HS image has been generated by applying a 7×7 Gaussian filter with zero mean and standard deviation $\sigma_{\mathbf{B}} = 1.7$ and by down-sampling every 4 pixels in both vertical and horizontal directions for each band of $\mathbf{X}$, as done in Section V-B1. Then, the PAN image has been obtained by averaging the first 50 HS bands. The HS and PAN images are both contaminated by additive Gaussian noises, whose SNRs are 40dB for all the bands. The reference image $\mathbf{X}$ is to be reconstructed from the coregistered HS and MS images.

The proposed FUMI algorithm and other state-of-the-art methods have been implemented to fuse the two observed images and to unmix the HS image. The fusion results and RMSE maps (averaged over all the bands) are shown in Figs. 2. Visually, FUMI give better fused images than the other methods. This result is confirmed by the RMSE maps, where the FUMI method offer much smaller errors than the other three methods. Furthermore, the quantitative fusion results reported in Table VIII are consistent with this conclusion as FUMI outperform the other methods for all the fusion metrics. Regarding the computation time, FUMI cost more than the other two methods, mainly due to the alternating update of the endmembers and abundances and also the ADMM updates within the alternating updates.

The unmixed endmembers and abundance maps are displayed in Figs. 3 and 4 whereas quantitative unmixing results are reported in Table IX. For endmember estimation, compared with the estimation used for initialization, all the methods have improved the accuracy of endmembers. FUMI offers the best endmember and abundance estimation results. This gives evidence that the estimation of endmembers benefits from being updated jointly with abundances, thanks to the complementary spectral and spatial information contained in the HS and high resolution MS images.

TABLE VI: Fusion Performance for Synthetic HS+PAN dataset: RSNR (in dB), UIQI, SAM (in degree), ERGAS, DD (in 10^{-2}) and time (in second).

Methods	RSNR	UIQI	SAM	ERGAS	DD	Time
Berne [22]	22.54±1.69	0.8836±0.0507	2.63±0.62	2.12±0.44	3.32±0.79	7.62±2.24
Yokoya [15]	26.23±0.57	0.9421±0.0204	1.90±0.23	1.39±0.08	2.10±0.19	10.78±0.52
Lanaras [26]	26.79±0.56	0.9476±0.0194	1.81±0.23	1.31±0.08	1.96±0.20	**4.38±0.92**
FUMI	**27.64±0.81**	**0.9587±0.0180**	**1.60±0.27**	**1.19±0.11**	**1.75±0.27**	15.79±3.41

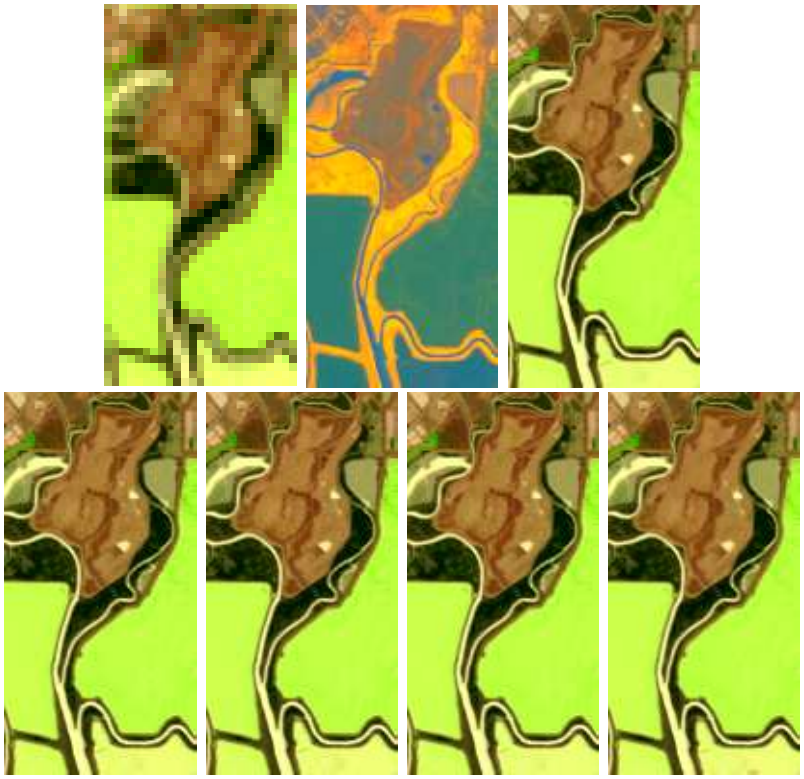

Fig. 2: Hyperspectral and multispectral fusion results (Moffett dataset): (Top 1) HS image. (Top 2) MS image. (Top 3) Reference image. (Bottom 1) Berne's method. (Bottom 2) Yokoya's method. (Bottom 3) Lanaras' method (Bottom 4) Proposed FUMI.

TABLE VIII: Fusion Performance for Moffett HS+MS dataset: RSNR (in dB), UIQI, SAM (in degree), ERGAS, DD (in 10^{-2}) and time (in second).

Methods	RSNR	UIQI	SAM	ERGAS	DD	Time
Berne [22]	22.55	0.9832	2.54	2.30	5.06	**13.2**
Yokoya [15]	23.74	0.9873	2.52	2.00	4.66	20.2
Lanaras [26]	25.53	0.9913	2.46	1.60	4.06	23.5
FUMI	**26.02**	**0.9919**	**1.96**	**1.53**	**3.51**	52.8

TABLE IX: Unmixing Performance for Moffett HS+MS dataset: $\mathrm{SAM_M}$ (in degree), $\mathrm{NMSE_M}$ (in dB) and $\mathrm{NMSE_A}$ (in dB).

Methods	$\mathrm{SAM_M}$	$\mathrm{NMSE_M}$	$\mathrm{NMSE_A}$
Initialization	16.90	-7.10	\
Berne [22]	11.66	-6.94	-4.41
Yokoya [15]	12.03	**-9.00**	-5.17
Lanaras [26]	12.42	-8.26	-4.55
FUMI	**10.09**	**-9.00**	**-6.45**

2) HS and PAN image fusion: In this section, we test the proposed algorithm on HS and PAN image fusion. The PAN image is obtained by averaging the first 50 bands of the reference image plus Gaussian noise (SNR is 40dB). Due to the space limitation, the corresponding quantitative fusion and unmixing results are reported in Tables X and XI and the visual results have been omitted. These results are consistent with the analysis associated with the Moffet HS+MS dataset. For fusion, FUMI outperforms the other methods with respect to all quality measures. In terms of unmixing, FUMI also outperforms the others for both endmember and abundance estimations, due to the alternating update of endmembers and abundances.

TABLE X: Fusion Performance for Moffett HS+PAN dataset: RSNR (in dB), UIQI, SAM (in degree), ERGAS, DD (in 10^{-2}) and time (in second).

Methods	RSNR	UIQI	SAM	ERGAS	DD	Time
Berne [22]	15.55	0.8933	6.20	4.82	1.28	14.6
Yokoya [15]	17.02	0.9330	4.67	3.96	1.00	18.0
Lanaras [26]	17.92	0.9454	4.45	3.56	0.91	**4.2**
FUMI	**18.50**	**0.9508**	**3.66**	**3.31**	**0.79**	46.6

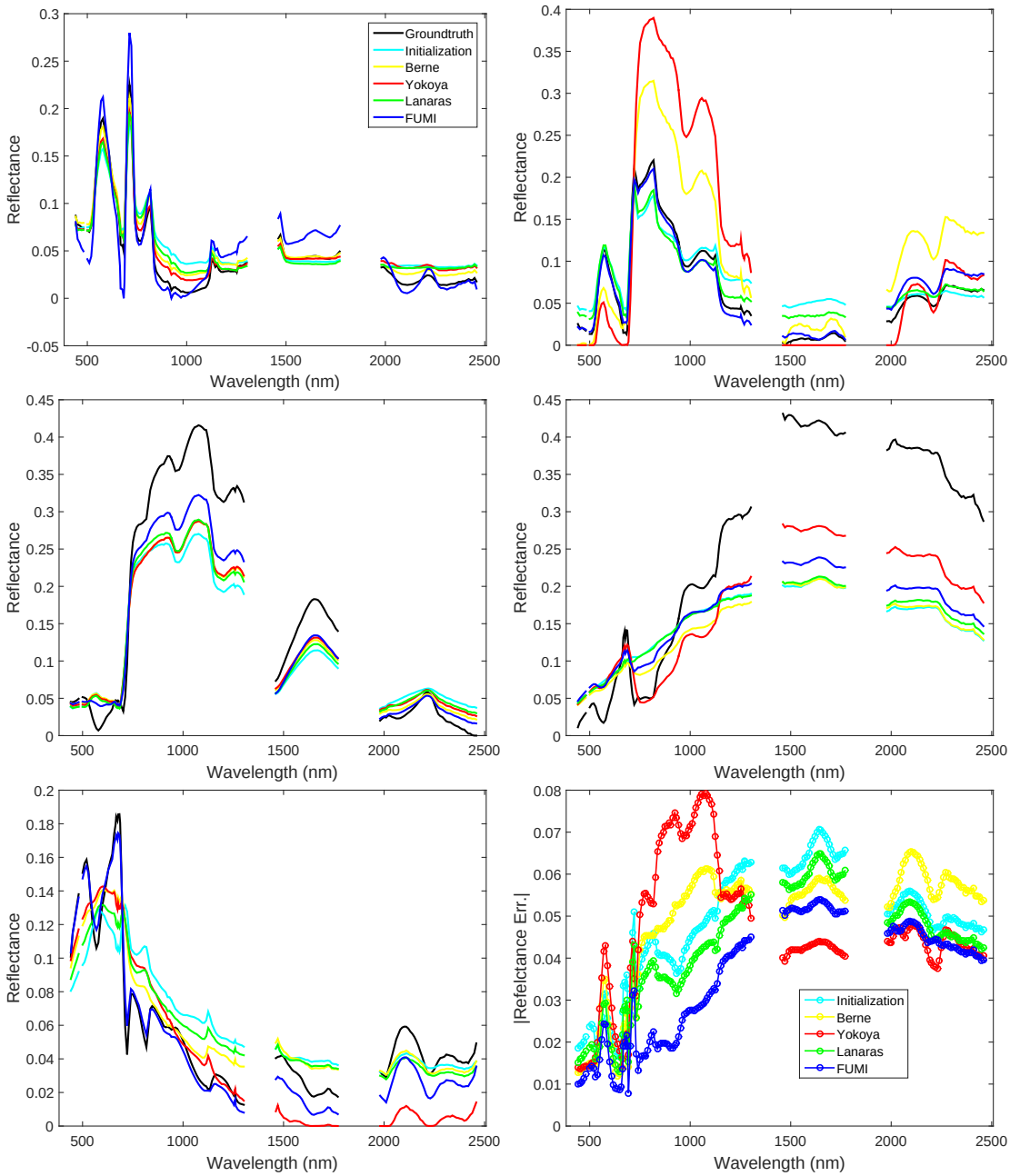

Fig. 3: Unmixed endmembers for Moffett HS+MS dataset: (Top, middle and bottom left) Estimated five endmembers and their ground truth. (Bottom right) Sum of absolute values of all endmember errors as a function of wavelength.

TABLE XI: Unmixing Performance for Moffett HS+PAN dataset: SAM_M (in degree), NMSE_M (in dB) and NMSE_A (in dB).

Methods	SAM_M	NMSE_M	NMSE_A
Initialization	16.90	-7.10	\
Berne [22]	11.66	-6.94	-5.18
Yokoya [15]	13.43	-7.92	-5.14
Lanaras [26]	13.59	-7.65	-3.25
FUMI	**9.65**	**-8.88**	**-6.01**

VI. Conclusion

This paper proposed a new algorithm based on spectral unmixing for fusing multi-band images. Instead of solving the associated problem approximately by decoupling two data terms, an algorithm to directly minimize the associated objective function has been designed. In this algorithm, the endmembers and abundances were updated alternatively, both using an alternating direction method of multipliers. The updates for abundances consisted of solving a Sylvester matrix equation and projecting onto a simplex. Thanks to the recently developed R-FUSE algorithm, this Sylvester equation was solved analytically thus efficiently, requiring no iterative update. The endmember updating was divided into two steps: a least square regression and a thresholding, that are both not computationally intensive. Numerical experiments showed that the proposed joint fusion and unmixing algorithm com-

pared competitively with three state-of-the-art methods, with the advantage of improving the performance for both fusion and unmixing. Future work will consist of incorporating the spatial and spectral degradation into the estimation framework. Extending the proposed method to other feature or decision level fusion will also be relevant.

REFERENCES

[1] Q. Wei, J. M. Bioucas-Dias, N. Dobigeon, J.-Y. Tourneret, and S. Godsill, "High-resolution hyperspectral image fusion based on spectral unmixing," in *Proc. IEEE Int. Conf. Inf. Fusion (FUSION)*, Heidelberg, Germany, July 2016, submitted.

[2] D. Landgrebe, "Hyperspectral image data analysis," *IEEE Signal Process. Mag.*, vol. 19, no. 1, pp. 17–28, Jan. 2002.

[3] K. Navulur, *Multispectral Image Analysis Using the Object-Oriented Paradigm*, ser. Remote Sensing Applications Series. Boca Raton, FL: CRC Press, 2006.

[4] R. Bacon, Y. Copin, G. Monnet, B. W. Miller, J. Allington-Smith, M. Bureau, C. M. Carollo, R. L. Davies, E. Emsellem, H. Kuntschner *et al.*, "The sauron project–i. the panoramic integral-field spectrograph," *Monthly Notices of the Royal Astronomical Society*, vol. 326, no. 1, pp. 23–35, 2001.

[5] S. J. Nelson, "Magnetic resonance spectroscopic imaging," *IEEE Engineering Med. Biology Mag.*, vol. 23, no. 5, pp. 30–39, 2004.

[6] C.-I. Chang, *Hyperspectral data exploitation: theory and applications*. New York: John Wiley & Sons, 2007.

[7] G. A. Shaw and H.-h. K. Burke, "Spectral imaging for remote sensing," *Lincoln Laboratory Journal*, vol. 14, no. 1, pp. 3–28, 2003.

[8] B. Aiazzi, L. Alparone, S. Baronti, A. Garzelli, and M. Selva, "25 years of pansharpening: a critical review and new developments," in *Signal and Image Processing for Remote Sensing*, 2nd ed., C. H. Chen, Ed. Boca Raton, FL: CRC Press, 2011, ch. 28, pp. 533–548.

[9] L. Loncan, L. B. Almeida, J. M. Bioucas-Dias, X. Briottet, J. Chanussot, N. Dobigeon, S. Fabre, W. Liao, G. Licciardi, M. Simoes, J.-Y. Tourneret, M. Veganzones, G. Vivone, Q. Wei, and N. Yokoya, "Hyperspectral pansharpening: a review," *IEEE Geosci. Remote Sens. Mag.*, vol. 3, no. 3, pp. 27–46, Sept. 2015.

[10] Q. Wei, N. Dobigeon, and J.-Y. Tourneret, "Bayesian fusion of multi-band images," *IEEE J. Sel. Topics Signal Process.*, vol. 9, no. 6, pp. 1117–1127, Sept. 2015.

[11] Q. Wei, J. Bioucas-Dias, N. Dobigeon, and J. Tourneret, "Hyperspectral and multispectral image fusion based on a sparse representation," *IEEE Trans. Geosci. Remote Sens.*, vol. 53, no. 7, pp. 3658–3668, Jul. 2015.

[12] M. Simoes, J. Bioucas-Dias, L. Almeida, and J. Chanussot, "A convex formulation for hyperspectral image superresolution via subspace-based regularization," *IEEE Trans. Geosci. Remote Sens.*, vol. 53, no. 6, pp. 3373–3388, Jun. 2015.

[13] B. Zhukov, D. Oertel, F. Lanzl, and G. Reinhackel, "Unmixing-based multisensor multiresolution image fusion," *IEEE Trans. Geosci. Remote Sens.*, vol. 37, no. 3, pp. 1212–1226, May 1999.

[14] M. T. Eismann and R. C. Hardie, "Application of the stochastic mixing model to hyperspectral resolution enhancement," *IEEE Trans. Geosci. Remote Sens.*, vol. 42, no. 9, pp. 1924–1933, Sep. 2004.

[15] N. Yokoya, T. Yairi, and A. Iwasaki, "Coupled nonnegative matrix factorization unmixing for hyperspectral and multispectral data fusion," *IEEE Trans. Geosci. Remote Sens.*, vol. 50, no. 2, pp. 528–537, 2012.

[16] Z. An and Z. Shi, "Hyperspectral image fusion by multiplication of spectral constraint and NMF," *Optik-International Journal for Light and Electron Optics*, vol. 125, no. 13, pp. 3150–3158, 2014.

[17] B. Huang, H. Song, H. Cui, J. Peng, and Z. Xu, "Spatial and spectral image fusion using sparse matrix factorization," *IEEE Trans. Geosci. Remote Sens.*, vol. 52, no. 3, pp. 1693–1704, 2014.

[18] L. Loncan, J. CHANUSSOT, S. FABRE, and X. BRIOTTET, "Hyperspectral pansharpening based on unmixing techniques," in *Proc. IEEE GRSS Workshop Hyperspectral Image SIgnal Process.: Evolution in Remote Sens. (WHISPERS)*, Tokyo, Japan, June 2015.

[19] E. Wycoff, T.-H. Chan, K. Jia, W.-K. Ma, and Y. Ma, "A non-negative sparse promoting algorithm for high resolution hyperspectral imaging," in *Proc. IEEE Int. Conf. Acoust., Speech, and Signal Processing (ICASSP)*. Vancouver, Canada: IEEE, 2013, pp. 1409–1413.

[20] Y. Zhang, S. De Backer, and P. Scheunders, "Noise-resistant wavelet-based Bayesian fusion of multispectral and hyperspectral images," *IEEE Trans. Geosci. Remote Sens.*, vol. 47, no. 11, pp. 3834 –3843, Nov. 2009.

[21] R. Kawakami, J. Wright, Y.-W. Tai, Y. Matsushita, M. Ben-Ezra, and K. Ikeuchi, "High-resolution hyperspectral imaging via matrix factorization," in *Proc. IEEE Int. Conf. Comp. Vision and Pattern Recognition (CVPR)*. Providence, USA: IEEE, Jun. 2011, pp. 2329–2336.

[22] O. Berne, A. Helens, P. Pilleri, and C. Joblin, "Non-negative matrix factorization pansharpening of hyperspectral data: An application to mid-infrared astronomy," in *Proc. IEEE GRSS Workshop Hyperspectral Image SIgnal Process.: Evolution in Remote Sens. (WHISPERS)*, Reykjavik, Iceland, Jun. 2010, pp. 1–4.

[23] X. He, L. Condat, J. Bioucas-Dias, J. Chanussot, and J. Xia, "A new pansharpening method based on spatial and spectral sparsity priors," *IEEE Trans. Image Process.*, vol. 23, no. 9, pp. 4160–4174, Sep. 2014.

[24] J. Bieniarz, D. Cerra, J. Avbelj, P. Reinartz, and R. Müller, "Hyperspectral image resolution enhancement based on spectral unmixing and information fusion," in *Proc. ISPRS Hannover Workshop 2011: High-Resolution Earth Imaging for Geospatial Information*, Hannover, Germany, 2011.

[25] Z. Zhang, Z. Shi, and Z. An, "Hyperspectral and panchromatic image fusion using unmixing-based constrained nonnegative matrix factorization," *Optik-International Journal for Light and Electron Optics*, vol. 124, no. 13, pp. 1601–1608, 2013.

[26] C. Lanaras, E. Baltsavias, and K. Schindler, "Hyperspectral super-resolution by coupled spectral unmixing," in *Proc. IEEE Int. Conf. Comp. Vision (ICCV)*, Santiago, Chile, Dec. 2015, pp. 3586–3594.

[27] J. Bioucas-Dias, A. Plaza, N. Dobigeon, M. Parente, Q. Du, P. Gader, and J. Chanussot, "Hyperspectral unmixing overview: Geometrical, statistical, and sparse regression-based approaches," *IEEE J. Sel. Topics Appl. Earth Observ. Remote Sens.*, vol. 5, no. 2, pp. 354–379, Apr. 2012.

[28] N. Yokoya, N. Mayumi, and A. Iwasaki, "Cross-calibration for data fusion of EO-1/Hyperion and Terra/ASTER," *IEEE J. Sel. Topics Appl. Earth Observ. Remote Sens.*, vol. 6, no. 2, pp. 419–426, 2013.

[29] I. Amro, J. Mateos, M. Vega, R. Molina, and A. K. Katsaggelos, "A survey of classical methods and new trends in pansharpening of multispectral images," *EURASIP J. Adv. Signal Process.*, vol. 2011, no. 79, pp. 1–22, 2011.

[30] M. González-Audícana, J. L. Saleta, R. G. Catalán, and R. García, "Fusion of multispectral and panchromatic images using improved IHS and PCA mergers based on wavelet decomposition," *IEEE Trans. Geosci. Remote Sens.*, vol. 42, no. 6, pp. 1291–1299, 2004.

[31] R. C. Hardie, M. T. Eismann, and G. L. Wilson, "MAP estimation for hyperspectral image resolution enhancement using an auxiliary sensor," *IEEE Trans. Image Process.*, vol. 13, no. 9, pp. 1174–1184, Sep. 2004.

[32] R. Molina, A. K. Katsaggelos, and J. Mateos, "Bayesian and regularization methods for hyperparameter estimation in image restoration," *IEEE Trans. Image Process.*, vol. 8, no. 2, pp. 231–246, 1999.

[33] R. Molina, M. Vega, J. Mateos, and A. K. Katsaggelos, "Variational posterior distribution approximation in Bayesian super resolution reconstruction of multispectral images," *Applied and Computational Harmonic Analysis*, vol. 24, no. 2, pp. 251 – 267, 2008.

[34] Y. Zhang, A. Duijster, and P. Scheunders, "A Bayesian restoration approach for hyperspectral images," *IEEE Trans. Geosci. Remote Sens.*, vol. 50, no. 9, pp. 3453 –3462, Sep. 2012.

[35] Q. Wei, N. Dobigeon, and J.-Y. Tourneret, "Bayesian fusion of hyperspectral and multispectral images," in *Proc. IEEE Int. Conf. Acoust., Speech, and Signal Processing (ICASSP)*, Florence, Italy, May 2014.

[36] N. Yokoya and A. Iwasaki, "Hyperspectral and multispectral data fusion mission on hyperspectral imager suite (HISUI)," in *Proc. IEEE Int. Conf. Geosci. Remote Sens. (IGARSS)*, Melbourne, Australia, Jul. 2013, pp. 4086–4089.

[37] M.-D. Iordache, J. Bioucas-Dias, and A. Plaza, "Sparse unmixing of hyperspectral data," *IEEE Trans. Geosci. Remote Sens.*, vol. 49, no. 6, pp. 2014–2039, Jun. 2011.

[38] Q. Wei, J. Bioucas-Dias, N. Dobigeon, and J.-Y. Tourneret, "Fast spectral unmixing based on Dykstra's alternating projection," *IEEE Trans. Signal Process.*, submitted.

[39] J. Nascimento and J. Bioucas-Dias, "Vertex component analysis: A fast algorithm to unmix hyperspectral data," *IEEE Trans. Geosci. Remote Sens.*, vol. 43, no. 4, pp. 898–910, 2005.

[40] N. Dobigeon, S. Moussaoui, M. Coulon, J.-Y. Tourneret, and A. O. Hero, "Joint Bayesian endmember extraction and linear unmixing for hyperspectral imagery," *IEEE Trans. Signal Process.*, vol. 57, no. 11, pp. 4355–4368, 2009.

[41] J. Li and J. Bioucas-Dias, "Minimum Volume Simplex Analysis: A fast algorithm to unmix hyperspectral data," in *Proc. IEEE Int. Conf. Geosci. Remote Sens. (IGARSS)*, vol. 3, Boston, MA, Jul. 2008, pp. III – 250–III – 253.

[42] Q. Wei, N. Dobigeon, and J.-Y. Tourneret, "Bayesian fusion of multispectral and hyperspectral images using a block coordinate descent method," in *Proc. IEEE GRSS Workshop Hyperspectral Image SIgnal Process.: Evolution in Remote Sens. (WHISPERS)*, Tokyo, Japan, Jun. 2015.
[43] C. P. Robert, *The Bayesian Choice: from Decision-Theoretic Motivations to Computational Implementation*, 2nd ed., ser. Springer Texts in Statistics. New York, NY, USA: Springer-Verlag, 2007.
[44] A. Gelman, J. B. Carlin, H. S. Stern, D. B. Dunson, A. Vehtari, and D. B. Rubin, *Bayesian data analysis*, 3rd ed. Boca Raton, FL: CRC press, 2013.
[45] D. P. Bertsekas, *Nonlinear programming*. Athena Scientific, 1999.
[46] Q. Wei, N. Dobigeon, J.-Y. Tourneret, J. M. Bioucas-Dias, and S. Godsill, "R-FUSE: Robust fast fusion of multi-band images based on solving a Sylvester equation," submitted. [Online]. Available: http://arxiv.org/abs/1604.01818/
[47] N. Keshava and J. F. Mustard, "Spectral unmixing," *IEEE Signal Process. Mag.*, vol. 19, no. 1, pp. 44–57, Jan. 2002.
[48] J. M. Bioucas-Dias and J. M. Nascimento, "Hyperspectral subspace identification," *IEEE Trans. Geosci. Remote Sens.*, vol. 46, no. 8, pp. 2435–2445, 2008.
[49] S. Boyd, N. Parikh, E. Chu, B. Peleato, and J. Eckstein, "Distributed optimization and statistical learning via the alternating direction method of multipliers," *Foundations and Trends® in Machine Learning*, vol. 3, no. 1, pp. 1–122, 2011.
[50] J. Eckstein and D. P. Bertsekas, "On the Douglas-Rachford splitting method and the proximal point algorithm for maximal monotone operators," *Mathematical Programming*, vol. 55, no. 1-3, pp. 293–318, 1992.
[51] M. Held, P. Wolfe, and H. P. Crowder, "Validation of subgradient optimization," *Mathematical programming*, vol. 6, no. 1, pp. 62–88, 1974.
[52] C. Michelot, "A finite algorithm for finding the projection of a point onto the canonical simplex of $\mathbb{R}^n$," *J. Optimization Theory Applications*, vol. 50, no. 1, pp. 195–200, 1986.
[53] J. Duchi, S. Shalev-Shwartz, Y. Singer, and T. Chandra, "Efficient projections onto the ℓ_1 for learning in high dimensions," in *Proc. Int. Conf. Machine Learning (ICML)*, Helsinki, Finland, 2008, pp. 272–279.
[54] L. Condat, "Fast projection onto the simplex and the l1 ball," *Hal preprint: hal-01056171*, 2014.
[55] R. A. Horn and C. R. Johnson, *Matrix analysis*. Cambridge, UK: Cambridge university press, 2012.
[56] Q. Wei, N. Dobigeon, and J.-Y. Tourneret, "Fast fusion of multi-band images based on solving a Sylvester equation," *IEEE Trans. Image Process.*, vol. 24, no. 11, pp. 4109–4121, Nov. 2015.
[57] M. A. Veganzones, M. Simões, G. Licciardi, N. Yokoya, J. M. Bioucas-Dias, and J. Chanussot, "Hyperspectral super-resolution of locally low rank images from complementary multisource data," *IEEE Trans. Image Process.*, vol. 25, no. 1, pp. 274–288, Jan 2016.
[58] J. Plaza, E. M. Hendrix, I. García, G. Martín, and A. Plaza, "On endmember identification in hyperspectral images without pure pixels: A comparison of algorithms," *J. Math. Imag. Vision*, vol. 42, no. 2-3, pp. 163–175, 2012.
[59] M. E. Winter, "N-FINDR: an algorithm for fast autonomous spectral end-member determination in hyperspectral data," in *Proc. SPIE Imaging Spectrometry V*, M. R. Descour and S. S. Shen, Eds., vol. 3753, no. 1. SPIE, 1999, pp. 266–275.
[60] T.-H. Chan, W.-K. Ma, A. Ambikapathi, and C.-Y. Chi, "An optimization perspective onwinter's endmember extraction belief," in *Proc. IEEE Int. Conf. Geosci. Remote Sens. (IGARSS)*. Vancouver, Canada: IEEE, Jul. 2011, pp. 1143–1146.
[61] R. O. Green, M. L. Eastwood, C. M. Sarture, T. G. Chrien, M. Aronsson, B. J. Chippendale, J. A. Faust, B. E. Pavri, C. J. Chovit, M. Solis *et al.*, "Imaging spectroscopy and the airborne visible/infrared imaging spectrometer (AVIRIS)," *Remote Sens. of Environment*, vol. 65, no. 3, pp. 227–248, 1998.

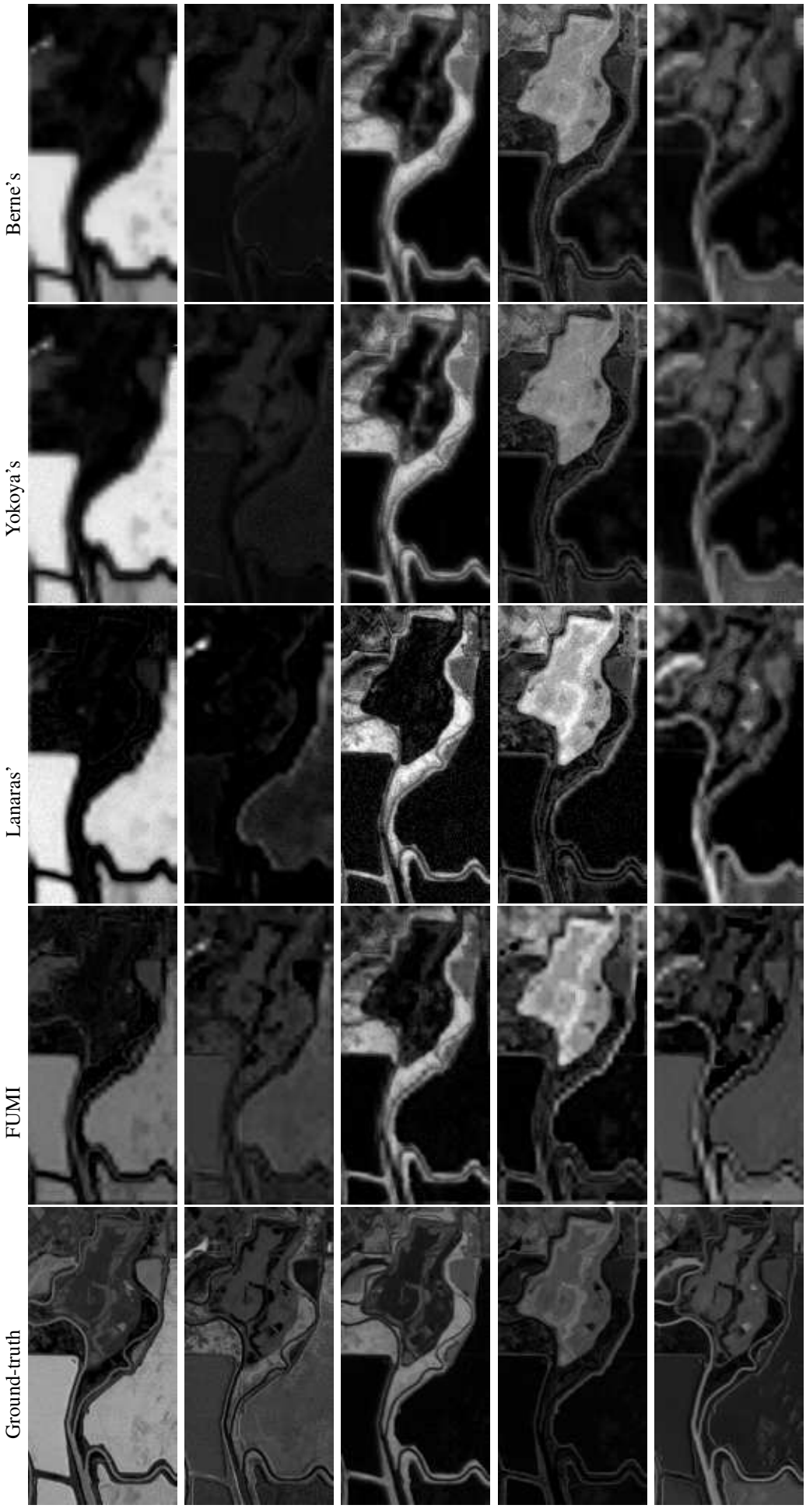

Fig. 4: Unmixed abundance maps for Moffett HS+MS dataset: Estimated abundance maps using (Row 1) Berne's method, (Row 2) Yokoya's method, (Row 3) Lanaras' method and (Row 4) proposed FUMI. (Row 5) Reference abundance maps. Note that abundances are linearly stretched between 0 (black) and 1 (white)